Research Square

Preprints are preliminary reports that have not undergone peer review.
They should not be considered conclusive, used to inform clinical practice,
or referenced by the media as validated information.

Multiaxial Mechanical and Environmental Characterization of Compression-Molded Sustainable Polyester Composites Reinforced with Virgin and Recycled Non-Woven Textiles

Eman Mustafa[1]
Suez University
Doaa H. Elgohary
doaaelgohary34@gmail.com
National Research Centre
Wael A. Hashima
Alexandria University
Mohamed I. A. Habba
Suez University

Article

Keywords: Non-woven polyester composites, Recycled PET, Compression molding, Tribological wear, Water absorption, Tensile behavior, Fiber bonding structure

Posted Date: November 9th, 2026

DOI: https://doi.org/10.21203/rs.3.rs-11440417/v1

License: This work is licensed under a Creative Commons Attribution 4.0 International License.
Read Full License

Additional Declarations: No competing interests reported.

Multiaxial Mechanical and Environmental Characterization of Compression-Molded Sustainable Polyester Composites Reinforced with Virgin and Recycled Non-Woven Textiles

Eman Mustafa[1], Doaa H. Elgohary*[2], Wael A. Hashima[3], Mohamed I. A. Habba[4]

[1]*Textile Department, Faculty of Technology and Education, Suez University, P.O. Box 43221, Suez, Egypt; Eman.Mustafa@ind.suezuni.edu.eg*

[2]*Department of Spinning and Weaving Engineering, Textile Research and Technology Institute, National Research Centre, 33 El Bohouth st. (Former El Tahrir St.), Dokki, Giza, P.O.12622, Egypt; doaaelgohary34@gmail.com*

[3]*Textile Engineering Department, Faculty of Engineering, Alexandria University, Egypt; wa_ahm2007@yahoo.com*

[4] *Mechanical Department, Faculty of Technology and Education, Suez University, P.O. Box 43221, Suez, Egypt; mohamed.atia@suezuniv.edu.eg*

***Correspondence**

Address correspondence to

e-mail: doaaelgohary34@gmail.com

Phone: +20 1003531623

ORCID: 0000-0002-7272-912X

Abstract

The increasing volume of post-consumer textile and polyethylene terephthalate (PET) waste has intensified interest in utilizing recycled fibers as reinforcements for structural polymer composites; however, the influence of fiber source and non-woven bonding structure on the resulting mechanical, tribological, and moisture-resistance performance remains insufficiently characterized. This study investigates non-woven-reinforced polyester composites fabricated from one virgin polyester preform (P) and three recycled non-woven preforms, two derived from textile waste (R1, R2) and one from recycled PET bottles (R3), varying in binder-fiber content and bonding method (needle punching alone versus combined needle punching and thermal bonding). The precursor fabrics were first characterized for air/water permeability, bursting strength, puncture resistance, and uniaxial strip/grab tensile behavior, after which composite panels of C, CP, CR1, CR2, and CR3 were fabricated via resin impregnation and compression molding and evaluated for bulk density, tensile properties with FE-SEM fracture-surface analysis, dry-sliding tribological wear, and water absorption/thickness swelling with surface morphology analysis. The results showed that composite tensile performance directly inherited the strength ranking of the precursor fabrics CR3 > CP > CR2 > CR1, with CR3 exhibiting the highest maximum tensile load, up to 2488 N, elongation, up to 11.26%, and toughness, up to 22,395 N across all loading directions, correlating with reduced fiber/matrix debonding observed by FE-SEM. Tribological testing revealed that CR2 exhibited the lowest volumetric wear loss across all applied loads ranging from 15 to 35 N, while unreinforced resin exhibited the highest, and CR1 consistently showed the greatest water absorption and thickness-swelling instability over a 10-day immersion period. These findings demonstrate that fiber source and thermal-bonding-derived interfacial integrity, rather than fiber loading fraction, govern the mechanical, tribological, and dimensional behavior of non-woven polyester composites, supporting the viability of recycled PET-bottle-derived non-woven reinforcements as sustainable, high-performance alternatives to virgin polyester fabrics in structural composite applications.

Keywords: Non-woven polyester composites; Recycled PET; Compression molding; Tribological wear; Water absorption; Tensile behavior; Fiber bonding structure

1. Introduction

The global transition toward circular manufacturing has placed increasing pressure on the polymer composites industry to reduce its dependence on virgin fiber reinforcements and to identify technically viable substitutes derived from post-consumer waste streams [1–4]. Two waste categories are of particular relevance to structural composite manufacturing: end-of-life textile fabrics, which continue to accumulate in landfills due to limited recycling infrastructure, and post-consumer polyethylene terephthalate (PET) bottles, whose large production volume and comparatively efficient collection systems make them an attractive feedstock for fiber reclamation [5–7]. Non-woven textile preforms, produced through needle punching, thermal bonding, or a combination of both, are especially well suited to valorizing these waste streams, since their manufacturing route can accommodate short, mechanically recycled, or chemically reprocessed fibers without requiring the precise fiber alignment demanded by woven or unidirectional reinforcements [8–12]. When consolidated with a thermosetting or thermoplastic matrix via compression molding, this nonwoven preforms yield composite panels suitable for semi-structural applications in the automotive, construction, and consumer goods sectors, where moderate mechanical performance is required alongside demonstrable sustainability benefits. Understanding how the fiber source and nonwoven bonding architecture govern the tensile, tribological, and hygroscopic behaviors of the resulting composite is not only a materials science question but also a prerequisite for the industrial adoption of recycled nonwoven reinforcements in place of virgin fabrics.

A substantial body of prior work has examined the relationship between non-woven manufacturing parameters and the mechanical performance of the resulting composites. Gnaba et al. [13] demonstrated, for flax/polypropylene non-woven-reinforced composites, that the mechanical properties of the consolidated composite are directly related to those of the dry non-woven reinforcement, with needle-

punching density and areal density identified as the dominant manufacturing-stage variables governing tensile and flexural behavior at both the fabric and composite scales; their work further established that the anisotropy observed between the machine and cross-machine directions at the composite level does not simply mirror that of the dry fabric, indicating that resin consolidation introduces an additional, direction-dependent modification to the inherited mechanical response. In parallel, reviews of fabric-reinforced natural fiber composites, such as that of Arumugam et al. [14], have consistently shown that continuous or structured fiber reinforcement (woven, knitted, or non-woven) outperforms randomly oriented short-fiber composites in strength and modulus, attributing this advantage to more effective fiber–matrix load transfer and mechanical interlock at the reinforcement scale, and underscoring that reinforcement architecture, rather than fiber chemistry alone, is a first-order determinant of composite mechanical performance. Regarding recycled PET as a matrix or fiber source, Monti et al. [15] demonstrated that fiber-reinforced composites based on recycled PET sourced from post-consumer bottles can achieve mechanical and impact performance suitable for technical applications when interfacial compatibilization is appropriately engineered, indicating that the processing history and molecular characteristics of the recycled feedstock, rather than the fact of its being "recycled" per se, govern the achievable composite performance. This finding is consistent with the broader circular economy literature on plastic recycling, which emphasizes that mechanical property retention in recycled-content composites depends critically on feedstock purity, degradation history, and the specific consolidation route employed, rather than on nominal reinforcement content. Separately, environmental durability, an essential but frequently underreported performance dimension for composites intended for outdoor, humid, or otherwise moisture-exposed service environments, has been shown to follow complex, non-Fickian uptake kinetics in fiber-reinforced polymers. Hassanpour and Karbhari [16] provide a comprehensive review of moisture-uptake mechanisms in fiber-reinforced composites, documenting that water ingress proceeds through a combination of diffusion, capillary transport along the fiber–matrix interface, and progressive interfacial debonding, with resulting dimensional changes

(swelling) that can depart substantially from simple Fickian predictions, particularly in composites with heterogeneous or porosity-variable reinforcement architectures such as non-woven mats. Despite this substantial foundation, a specific and practically important gap remains in literature. Existing studies have generally examined either the effect of non-woven manufacturing parameters on mechanical performance in isolation [13], or the mechanical viability of recycled-PET-based composites within a single performance domain, most commonly impact or tensile strength [15]. Few, if any, studies have directly compared virgin polyester non-woven fabric against multiple distinct classes of recycled non-woven reinforcement, specifically, textile-waste-derived fabrics processed by needle punching alone versus combined needle punching and thermal bonding, and PET-bottle-derived fabrics processed under the same combined bonding route, within a single, consistent compression-molding and characterization framework spanning tensile behavior, fracture micromechanics, dry-sliding tribological wear, and long-term water absorption and thickness-swelling response. This absence of an integrated, multi-domain comparison leaves an unresolved question of direct industrial relevance: whether the interfacial and structural advantages conferred by thermal bonding and PET-bottle fiber sourcing observed in isolated mechanical studies persist, attenuate, or interact differently when the same composite panels are subsequently subjected to tribological and hygroscopic service conditions.

Accordingly, the present study investigates the use of virgin and recycled polyester-based nonwoven textiles as reinforcement materials for sustainable polyester composites, with particular emphasis on the relationships among reinforcement origin, nonwoven architecture, and composite performance. Virgin polyester fibers, recycled textile waste, and recycled PET-derived polyester fibers were incorporated through different nonwoven fabrication and bonding configurations to establish a comparative experimental framework. The developed composites were systematically evaluated in terms of density, tensile behavior in different material orientations, fracture morphology, tribological wear performance, and water absorption and thickness changes under moisture exposure. The novelty of the present work lies in integrating these complementary performance domains within a common experimental framework

while simultaneously considering the effects of recycled feedstock origin and nonwoven architecture. In addition, the study extends the conventional performance-based evaluation of recycled composites by providing a quantitative material-inventory assessment of recycled-derived material incorporation, thereby linking waste utilization with the measured functional performance of the resulting composites. This integrated structure–performance approach provides a comprehensive basis for understanding how reinforcement source and nonwoven architecture influence the mechanical, tribological, and moisture-related behavior of polyester composites and supports the development of value-added composite materials from textile and PET waste streams.

2. Materials and Methods

This section outlines the experimental workflow adopted to develop and characterize non-woven-reinforced polyester composites, as summarized in Figure **1**. The study proceeded through four continuous stages: selection and baseline characterization of four commercial non-woven textile preforms of P, R1, R2, and R3; evaluation of their fluid-transport, multiaxial, and uniaxial tensile properties prior to consolidation; fabrication of the corresponding composite panels of C, CP, CR1, CR2, and CR3 via resin impregnation and compression molding; and finally, characterization of the consolidated panels encompassing bulk density, tensile behavior with fracture-surface analysis, tribological wear performance, and water absorption and thickness-swelling response. Each stage was conducted in accordance with the relevant ASTM standards, as detailed in the following subsections.

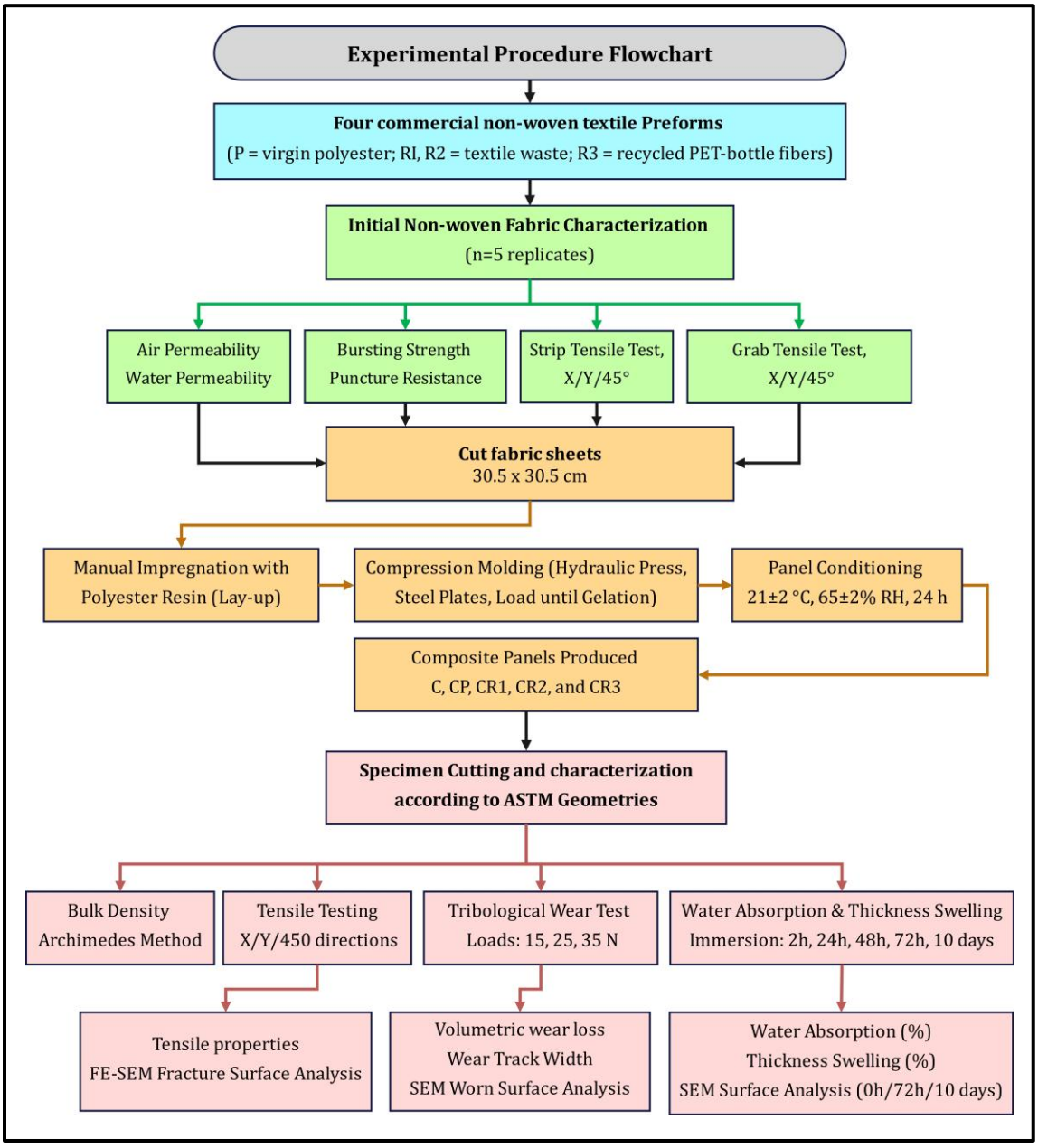


Figure 1. Flowchart of the experimental procedure, from nonwoven fabric characterization to composite fabrication and testing.

2.1. Initial materials

Table **1** summarizes the physical and structural specifications of the four distinct commercial non-woven textile preforms selected as the reinforcing phases for subsequent composite fabrication. To confirm a controlled-comparison baseline, all fabrics were selected to maintain a similar density profile of approximately 855 g/m². The selected materials comprised one available virgin polyester nonwoven fabric and three recycled nonwoven fabrics. Among the recycled samples, two were produced from post-consumer textile waste, while the third was

manufactured from recycled polyester fibers derived from PET bottles. The virgin nonwoven fabric (P) consisted of polyester staple fibers blended with sheath/core low-melting polyester binder fibers. It was initially bonded through needle punching, followed by thermal bonding to improve structural integrity. The recycled nonwoven fabrics derived from textile waste exhibited different bonding structures. Sample R1 was produced entirely by needle punching, whereas sample R2 incorporated both polyester staple fibers and 10–15% sheath/core low-melting binder fibers, and was therefore subjected to both needle punching and thermal bonding. The final sample (R3) was fabricated from recycled polyester fibers obtained from plastic (PET) bottles, also blended with 10–15% sheath/core low-melting binder fibers and processed using combined needle punching and thermal bonding. As shown in Table **1**, all samples possessed similar areal densities, while slight variations in thickness were observed depending on fiber composition and bonding method. All textile specimens were conditioned in a controlled-environment chamber for 24 hours, as per ASTM D1776, to ensure equilibrium moisture content prior to all measurements. This standard atmosphere for textile testing ensured consistency in comparative mechanical and physical performance evaluations across all fiber systems. After conditioning, each non-woven sample's areal density was determined in accordance with ASTM D3776, while material thickness was measured using the precision gauge methodology of ASTM D1777. Each test was conducted with at least five replicates to ensure statistically meaningful results.

Table 1. Physical and structural properties of the four-baseline nonwoven textile preform, including fiber raw material composition, bonding method, areal density, and average thickness.

Initial non-woven materials code	Description	Density (g/m^2)	Thickness (mm)
P	Virgin polyester fibers + Shealth/core low-melt polyester (10-15%)	855.27 ±7	6.52 ±0.15
R1	Textile waste	855.27 ±10	5.77 ±0.07
R2	Textile waste + Shealth/core low-melt polyester (10-15%)	855.27 ±19	6.13 ±0.14
R3	Recycled polyester fibers (Plastic bottles) + Shealth/core low melt polyester (10-15%)	855.27 ±5	6.09 ±0.25

2.2. Initial Non-Woven Textile Characterization

The physical, transport, and structural-mechanical properties of the initial non-woven preforms were characterized before resin consolidation to analyze their baseline performance and fluid permeability

behavior. Air permeability was measured in accordance with ASTM D737 using calibrated Toyoseki air permeability testing equipment. Each conditioned textile specimen was mounted into a circular test cell under standard mechanical clamping pressure to prevent edge leakage across the boundary zone of the cell. Airflow resistance was measured by monitoring the volumetric flow rate of air passing vertically through a known fabric test area at a constant regulated differential pressure head of 125 Pa. The water permeability of the porous preforms was measured under a constant head configuration according to ASTM D4491 to assess the volumetric liquid discharge capacity of the macroporous fibrous networks. The specimens were fully wetted to ensure complete saturation and remove any entrapped air before testing. The volume of water flowing perpendicular to the non-woven plane was monitored under controlled hydraulic gradient conditions, and the steady-state flow transport metrics were recorded in L/min. The multiaxial mechanical integrity and localized puncture performance of the preforms were determined using bursting and puncture tests to simulate the stresses generated during the consolidation of the mold. Bursting strength was evaluated using the hydraulic diaphragm method in compliance with ASTM D3786 using an SDL Atlas Hydraulic Bursting Strength Tester. The specimens were clamped over a flexible synthetic diaphragm, which was progressively expanded under hydraulic fluid pressure until localized rupture of the interlocking fiber network occurred. The peak bursting force (N) and failure displacement (mm) were recorded. The localized puncture resistance was evaluated according to ASTM D4833. A standardized flat-ended steel puncture probe was driven vertically through the center of the securely clamped nonwoven fabric at a constant crosshead displacement rate of 300 mm/min using a universal mechanical tester until penetration failure occurred. The uniaxial tensile properties of the fabrics were measured in multiple directions. Uniaxial strip tensile testing was performed in strict accordance with ASTM D5035 using a strip test configuration. Rectangular specimens with dimensions of 50 mm × 200 mm were prepared along the principal machine direction (Y-direction), cross-machine direction (X-direction), and an off-axis diagonal direction oriented at 45°. To assess the gripping and stress-concentration effects, parallel grab tensile tests were conducted in the X, Y, and 45° directions

according to ASTM D5034. For all characterization procedures, five replicates were tested for each sample group.

2.3. Non-Woven Composite Panels Fabrication

All non-woven fabrics were converted into non-woven composite panels, as shown in Figure **2**, using a consistent polyester resin lay-up and compression molding process. Initially, each non-woven fabric was cut into sheets of 30.5 × 30.5 cm. The composite lay-up was performed by manually impregnating each fabric layer with polyester resin to achieve uniform wet-out. The impregnated lay-ups were then placed between steel plates and transferred to a hydraulic compression system that applied a load of 12.5 tons. Pressure was maintained until resin gelation and sufficient consolidation were achieved [4,11]. Before testing, all fabricated nonwoven-based composite specimens were conditioned under standard laboratory conditions (21 ± 2°C and 65 ± 2% relative humidity) for 24 h to minimize the influence of environmental factors on the experimental results and ensure consistent, reproducible testing. Table **2** lists the designation codes assigned to the consolidated composite panels, along with their respective baseline fabric reinforcements, processing environments, and resulting gravimetric fiber-to-resin mass ratios. To maintain systemic traceability, each composite sample was designated with the prefix "C-" followed by the corresponding baseline fabric code: CP, CR1, CR2, or CR3.

Table 2. Non-woven composite panels sample codes.

No.	Composites code	Structure
1.	C	Resin
2.	CP	Resin + P
3.	CR1	Resin + R1
4.	CR2	Resin + R2
5.	CR3	Resin + R3



Figure 2. Composite panel preparation

2.4. Non-woven Composite Characterization Procedures

The composite sheets were carefully cut (Figure **3**) into the required geometries and dimensions according to the relevant ASTM standard specifications for each characterization method, as shown in Figure **4**. Specimen preparation also included precise trimming of the sample edges and dimensional verification to reduce the experimental variability associated with the nonwoven composite structures. The prepared samples were subjected to mechanical, tribological, physical, and morphological evaluations to comprehensively assess the overall performance and structural integrity of the developed composites.

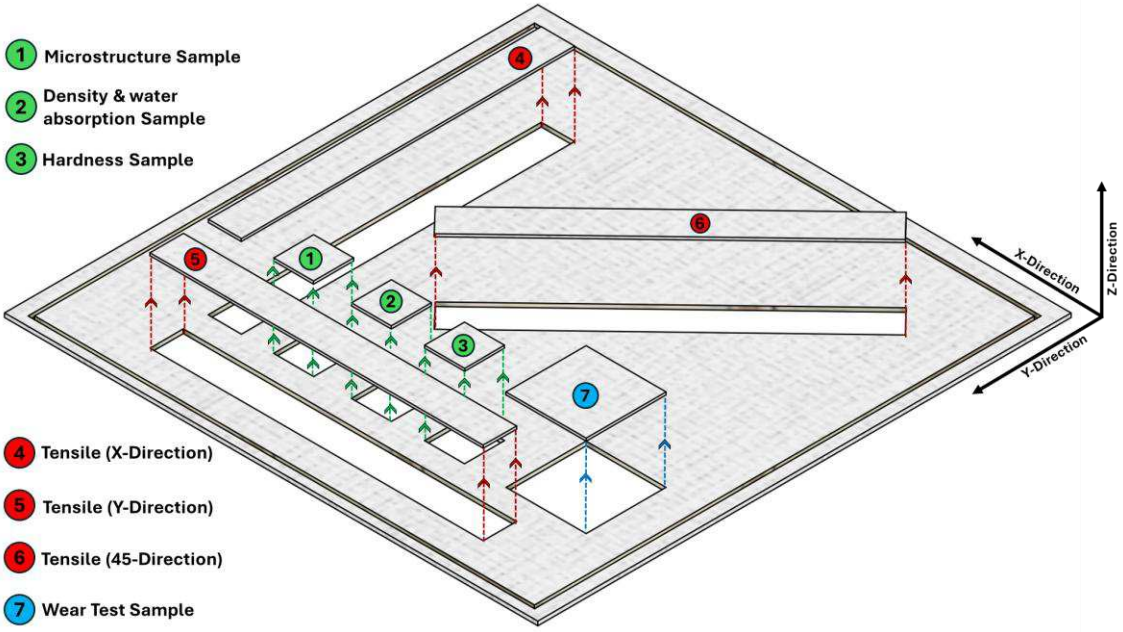


Figure 3. Schematic of three-dimensional isometric extraction demonstrating precise multiaxial specimen-cutting configurations along the Y, X, and 45° directions.

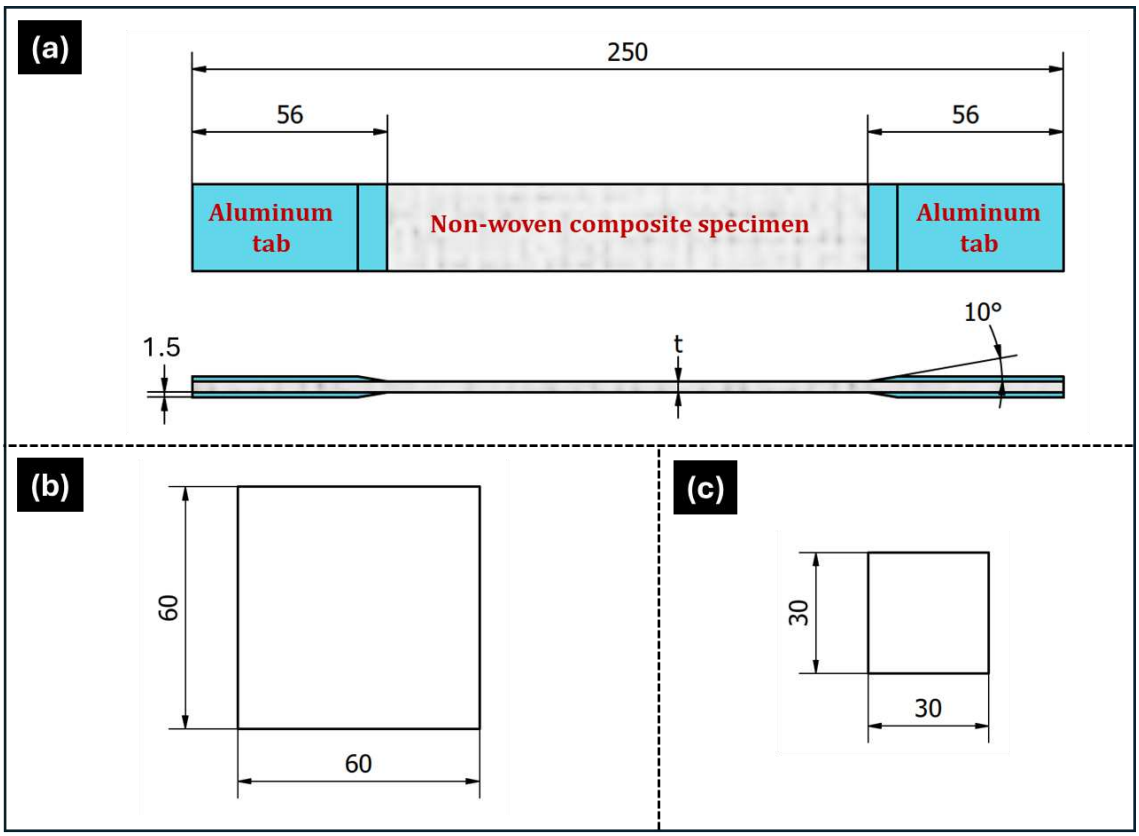


Figure 4. Detailed dimensions and geometric profiles of the prepared characterization specimens.

The experimental bulk density (ρ_e) The weight of the consolidated nonwoven composite panels was determined using the Archimedes method in accordance with ASTM D792. Three measurements were performed for each produced sample. Specimen weights were recorded in an ambient air environment and subsequently, when fully immersed in distilled water at 23 °C, using a high-precision analytical balance with an accuracy of 0.0001 g. Composite tensile properties were evaluated using a WDW-300D universal testing machine (30-ton capacity, Guangdong, China). Specimens were prepared following ASTM D3039 and tested along the X, Y, and 45° directions to capture the anisotropic response of the non-woven-reinforced panels. Tests were conducted at an ambient laboratory temperature with axial loading applied at a controlled displacement rate, and stress–strain curves were recorded continuously using the machine's digital acquisition system. After a tensile fracture, the specimen panels were examined by FE-SEM along each loading direction to investigate the fracture mechanisms at the fracture surface of each selected specimen. The tribological wear behavior of composite materials was evaluated according to ASTM G133-02 (dry sliding pin-on-flat configuration). A specialized EGY-TEF-M1 wear tester (Faculty of Technology and Education, Suez University, Egypt) was used for all experiments. The counter body was a 10 mm-diameter AISI 52100 steel ball with a surface hardness of 63 HRC and a roughness of 0.05 μm. Tests were conducted under controlled load and sliding distance, and the wear track morphology was evaluated post-test. The mass loss of the samples was measured before and after testing to calculate the wear rate. After wear testing, selected worn specimens from each sample group were examined by FE-SEM to characterize the worn surface morphology at each applied load. Water absorption and dimensional stability were evaluated in accordance with ASTM D1037-2006. Composite specimens (3 × 3 cm^2) were oven-dried and weighed (W_1), then immersed in distilled water at 20 ± 2°C for 2 h, 24 h, 48 h, and 72 h. After each immersion period, the samples were removed, surface-dried, weighed (W_2), and the thickness was recorded ($T_1 \rightarrow T_2$). Water absorption (%) and thickness swelling (%) were calculated using Eq. 1 and Eq. 2, respectively.

$$\text{Water Absorption (\%)} = \left(\frac{W_2 - W_1}{W_1}\right) \times 100 \rightarrow Eq.1$$

$$\text{Thickness Swelling (\%)} = \left(\frac{T_2 - T_1}{T_1}\right) \times 100 \rightarrow Eq.2$$

To assess the progression of moisture-induced surface degradation, selected immersed specimens were examined by FE-SEM before immersion (0 h) and after 72 h and 10 days of exposure, to characterize the surface morphology at each immersion interval.

The material inventory of the developed composite systems was estimated to quantify the incorporation of recycled-derived material. The fabricated composite panels had dimensions of 30.5 × 30.5 cm, corresponding to a panel area of 0.093025 m². The average composite thickness was approximately 2.2 mm; because the differences in thickness among the fabricated panels were relatively small, this average value was used for the material-inventory estimation. The experimentally determined composite densities and reinforcement mass fractions were used as the basis for the calculations. The reinforcement fractions were 32.6, 29.7, 33.9, and 30.6 wt% for CP, CR1, CR2, and CR3, respectively. The panel volume was calculated as:

$$V = A \times t \rightarrow Eq.3$$

The estimated panel mass was subsequently calculated as:

$$m_{panel} = \rho V \rightarrow Eq.4$$

The reinforcement mass was calculated according to:

$$m_{reinforcement} = m_{panel} \times w_f \rightarrow Eq.5$$

For the recycled systems, the recycled-derived material was estimated using:

$$m_{recycled} = m_{reinforcement} \times f_{recycled} \rightarrow Eq.6$$

where $f_{recycled}$was considered as 100% for R1 and 85–90% for R2 and R3 according to the composition of the corresponding nonwoven reinforcements. Finally, the recycled-derived material per unit area was calculated as:

$$M_{recycled} = \frac{m_{recycled}}{A} \rightarrow Eq.7$$

3. Results and Discussion

3.1. Initial Materials Characterization

Before proceeding to composite production, the used nonwoven fabric samples were characterized to evaluate fluid permeability, multiaxial mechanical, and uniaxial tensile properties. Air and water permeability were measured and compared across all samples (Figure **5**), while bursting strength and puncture resistance were evaluated to illustrate the behavior of the fabrics to multidirectional and localized loading conditions (Figure **6**). The uniaxial tensile behavior was conducted using both the strip and grab test configurations along the principal directions Y, X, and 45°, with results reported in Figure **7** and Figure **8**, respectively.

In terms of fluid transport properties, notable differences in air permeability were observed among the samples, whereas water permeability values remained comparatively consistent, as shown in Figure **5**. Sample P showed the highest air permeability of 133.8 ± 6.69 $cm^3/cm^2 \cdot s$, followed by R2 (115.7 ± 5.79 $cm^3/cm^2 \cdot s$), R3 (91.99 ± 4.6 $cm^3/cm^2 \cdot s$), and R1 (58.95 ± 2.95 $cm^3/cm^2 \cdot s$), showing a reduction of approximately 55.9% relative to P. These results suggest that the presence of sheath–core low-melt binder fibers, along with the corresponding thermal bonding mechanism, influenced the pore structure and airflow resistance. In contrast, water permeability values across all tested initial materials ranged from 0.70 to 0.73 L/min, with overlapping error limits indicating no statistically significant differences. This behavior indicates that water flow through these nonwoven structures was not significantly influenced by the fiber source or bonding method.

In terms of resistance to multiaxial and localized loading, substantial differences among the initial non-woven samples were observed in the bursting strength and puncture resistance tests, as presented in Figure **6**. Sample R3, fabricated from recycled PET-bottle-derived polyester fibers blended with sheath–core low-melt binder fibers and processed via combined needle punching and thermal bonding, achieved

the highest bursting strength of 2613.33 ± 130.67 N and the highest puncture resistance of 944.07 ± 47.2 N. Sample P exhibited the second-highest bursting strength of 1956.73 ± 97.84 N and puncture resistance of 787.27 ± 39.36 N. In addition, sample P exhibited the highest displacement at burst failure of 5.07 ± 0.26 mm, indicating considerable deformation capacity before failure. Sample R1, comprising only needle-punched textile waste without binder fiber addition, exhibited the lowest bursting strength of 124.13 ± 6.21 N, representing a reduction of approximately 95.2% relative to R3. A remarkable difference in puncture resistance was observed, with R2 of 22.78 ± 1.14 N lower than R1 of 49.0 ± 2.45 (Figure 6), despite the incorporation of thermal binder fibers. This variation indicates that the bonding points introduced by thermal treatment in R2 created localized stress concentrations that facilitated early failure under the sharp, uniaxial loading mode of the puncture test.

The strip tensile test results revealed variations in the uniaxial load-bearing behavior of the initial nonwoven materials, depending on both fiber composition and testing direction, as shown in Figure **7**. Sample R3 showed the highest strip tensile strength across all three testing orientations (X, Y, and 45°), with 1701.93 ± 85.09 N in the Y-direction, 931.00 ± 46.55 N in the X-direction, and 1192.33 ± 59.62 N at 45°. Sample P obtained the second-highest values of 868.93 ± 43.44 N, 672.93 ± 34.95 N, and 699.07 ± 33.65 N in the Y, X, and 45° directions, respectively, with significant elongation of 127.33 ± 4.37% in the X direction, as shown in Figure **7**. Sample R1 recorded the lowest strip tensile strength, ranging from 9.8 to 12.2 N, a reduction of approximately 99.4% relative to R3 in the Y-direction, indicating highly deficient inter-fiber cohesion in the absence of binder fibers. The descending order of strip tensile strength in the Y-direction was R3 > P > R2 > R1. Directional anisotropy was evident in both R3 and P, with higher tensile strength in the Y-direction than in the X-direction, suggesting a preferential fiber orientation along the machine direction introduced during needle punching and thermal bonding. Elongation behavior followed a distinct pattern, with R2 recording the lowest elongation values across all directions, achieving 34.00 ± 1.7% in Y, 44.50 ± 1.2% in X, and 34.67 ± 1.73% at 45°, indicating that thermal bonding points limit fiber mobility and reduce extensibility within the textile waste-based fabric.

The grab tensile test results were closely aligned with the strip tensile test results, confirming the dominant influence of fiber composition and bonding efficiency on localized load-bearing performance, as shown in Figure **8**. Sample R3 showed the highest grab tensile strength of 1685.60 ± 84.28 N in Y, 1117.20 ± 55.86 N in X, and 1349.13 ± 67.46 N at 45°, followed by sample P with values of 1215.20 ± 60.76 N, 906.50 ± 48.18 N, and 963.67 ± 45.33 N in the corresponding directions. Sample R1 recorded the lowest grab tensile strength, ranging from 10.3 to 11.8 N across all directions, consistent with its highly deficient inter-fiber cohesion. Furthermore, R3 exhibited higher grab tensile strength at 45° of 1349.13 N than in the X-direction of 1117.20 N, as shown in Figure **8**, indicating that diagonal fiber interlocking contributes additional resistance under off-axis loading in thermally bonded PET-based nonwoven structures. The elongation behavior under the grab test configuration mirrored the strip test trends, with sample P recording the highest X-direction elongation of 92.33 ± 4.62% and R2 exhibiting the lowest elongation across all directions, confirming that thermal bonding in textile waste-based fabrics constrains fiber slippage and extensibility. The results of initial material characterizations indicate that fiber source, binder fiber content, and bonding method are the primary determinants of nonwoven fabric behavior, with recycled PET-based fibers combined with thermal bonding consistently yielding higher mechanical and physical properties across all tested conditions.

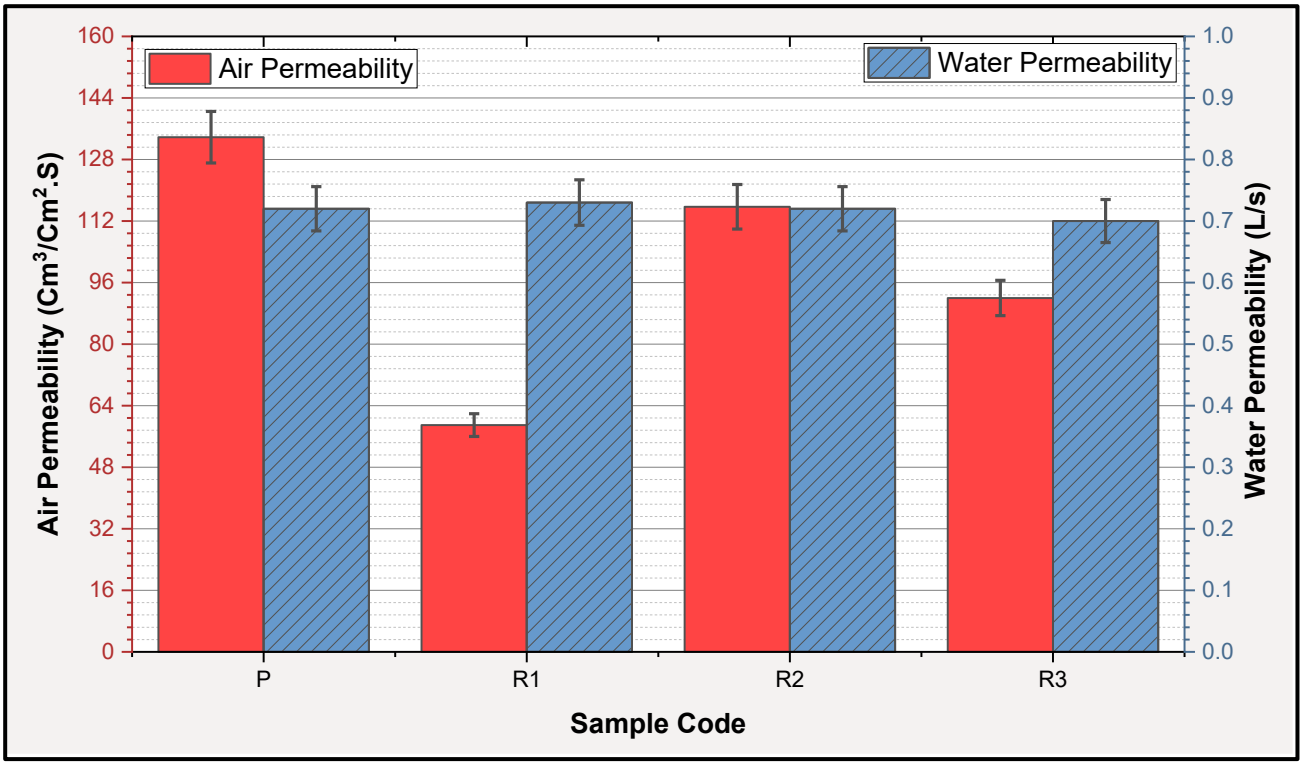


Figure 5. Air permeability and water permeability (L/sec) of four nonwoven fabric samples.

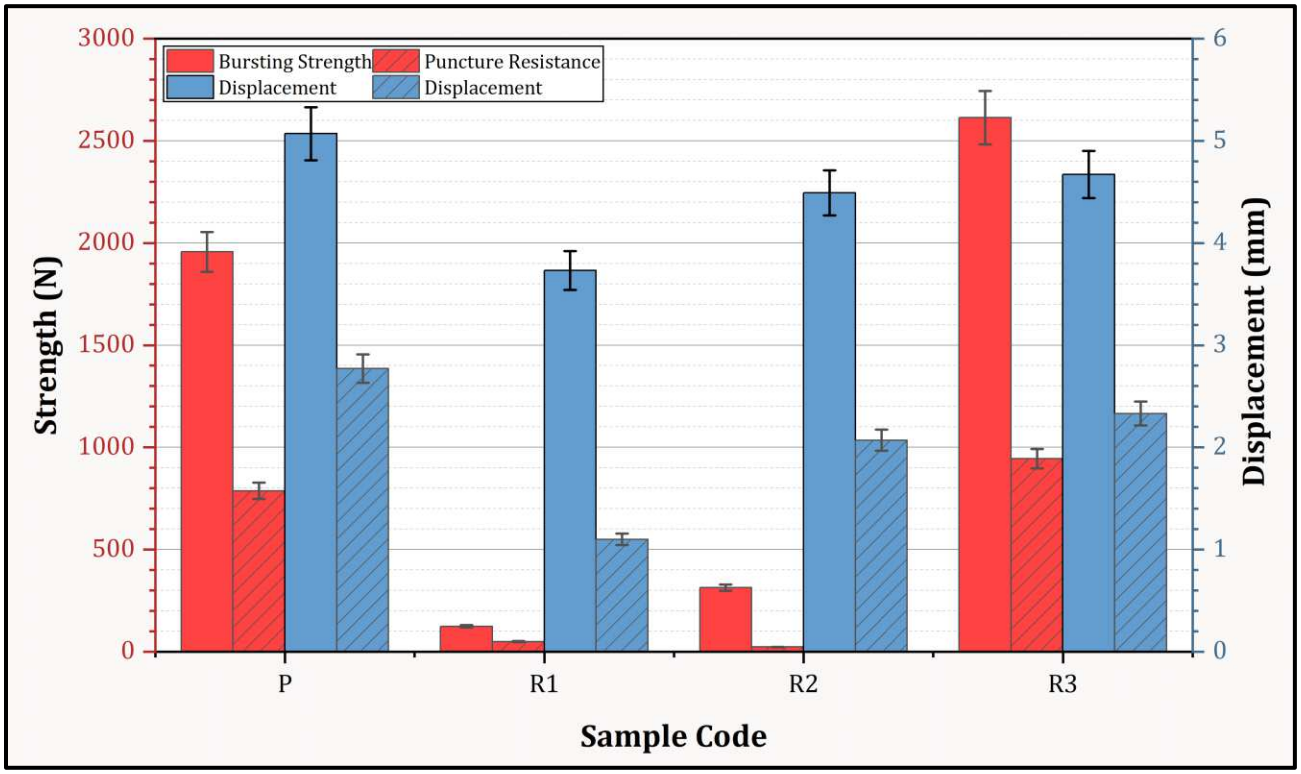


Figure 6. Bursting strength, displacement at burst, puncture resistance, and displacement at puncture for the four nonwoven fabric samples.

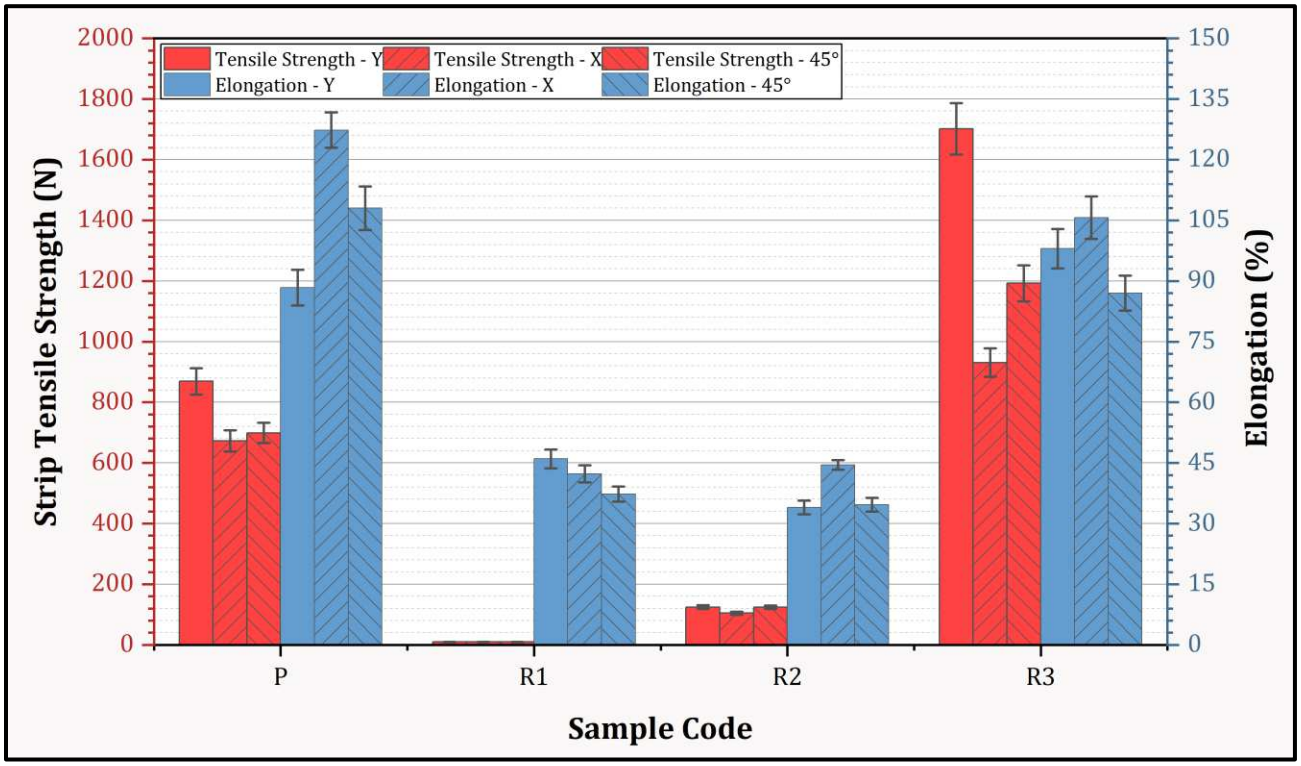


Figure 7. Strip tensile strength and elongation of the four nonwoven fabric samples along the X, Y, and 45° directions.

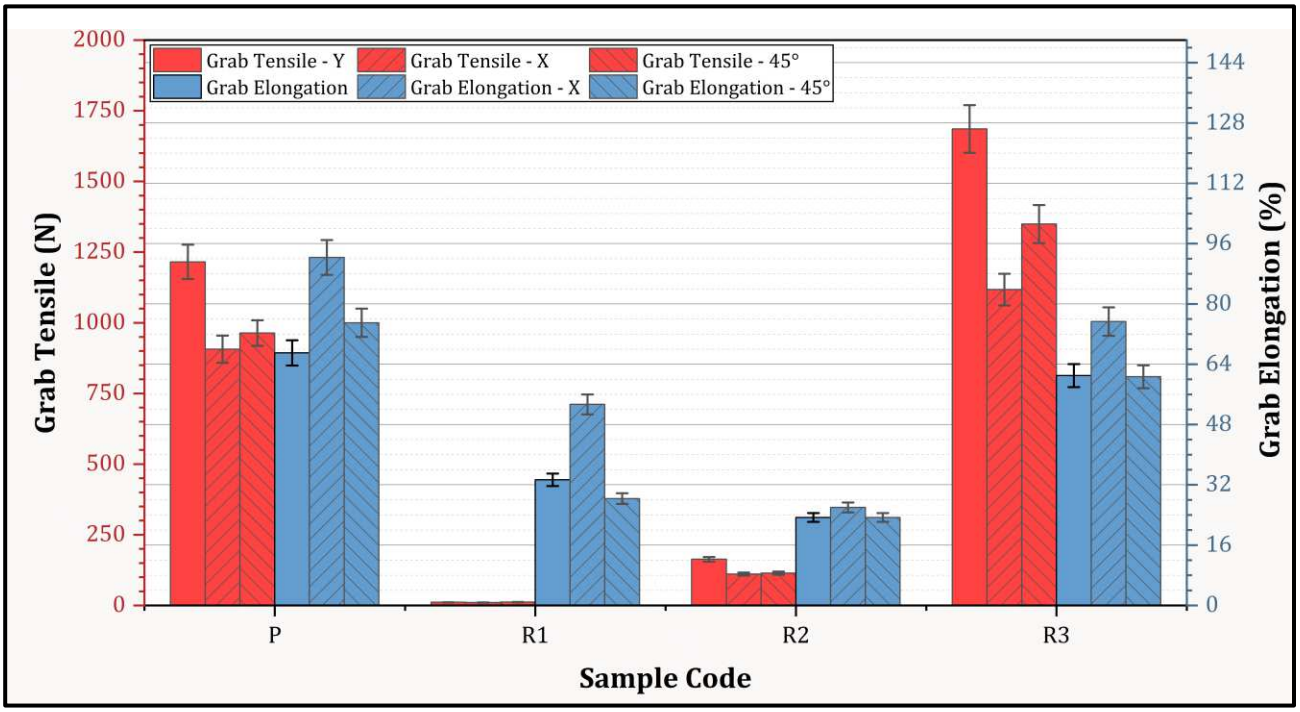


Figure 8. Grab tensile strength and elongation of the four non-woven fabric samples along the X, Y, and 45° directions.

3.2. Characterization of Composites

To provide a basis for evaluating the physical, mechanical, tribological, and water-resistance performance of the fabricated panels, the fiber-to-resin mass ratio of each composite was first determined following consolidation under a 12.5-ton compression load. As shown in Table **3**, all reinforced composites had similar fiber fractions, ranging from 29.7% for CR1 to 33.9% for CR2, while the corresponding resin contents ranged from 66.1% to 70.3%. This relatively narrow compositional range indicates that the differences in composite performance are primarily attributable to the characteristics of the non-woven reinforcement, namely, fiber source, structural integrity, and bonding condition, rather than to major variations in constituent proportions. The unreinforced polyester resin sample coded with "C" was included as a reference material with 100% resin content.

Table 3. Fiber-to-resin mass ratios of the non-woven composite panels fabricated under 12.5-ton compression, relative to the unreinforced resin panel C.

No.	Composites code	Fiber ratio (%)	Resin Ratio (%)
1.	C	0	100
2.	CP	32.6	67.4
3.	CR1	29.7	70.3
4.	CR2	33.9	66.1
5.	CR3	30.6	69.4

3.2.1. Bulk Density

The bulk densities of the unreinforced polyester resin and non-woven-reinforced composite panels are presented in Figure **9**. The unreinforced resin sample (C) exhibited the lowest density among all groups, measuring 1.1804±0.011 g/cm³. A clear trend emerged: all four non-woven-reinforced composites exhibited higher density than the unreinforced resin reference, indicating a higher shift in bulk density following the incorporation of non-woven fibrous reinforcement. Among the reinforced panels, CR3

displayed the highest density, at 1.2477±0.010 g/cm³, followed by CR1 at 1.2327±0.009 g/cm³ and CP at 1.2315±0.015 g/cm³, which were closely clustered together. CR2 exhibited the lowest density among the reinforced composites, at 1.2033±0.012 g/cm³, representing a significant deviation from the otherwise narrow range observed for CP and CR1. The density of the composite panels ranged from 1.2033±0.012 g/cm³ for CR2 to 1.2477±0.010 g/cm³ for CR3, a spread of approximately 0.0444 g/cm³ across the reinforced group, as shown in Figure **9**.

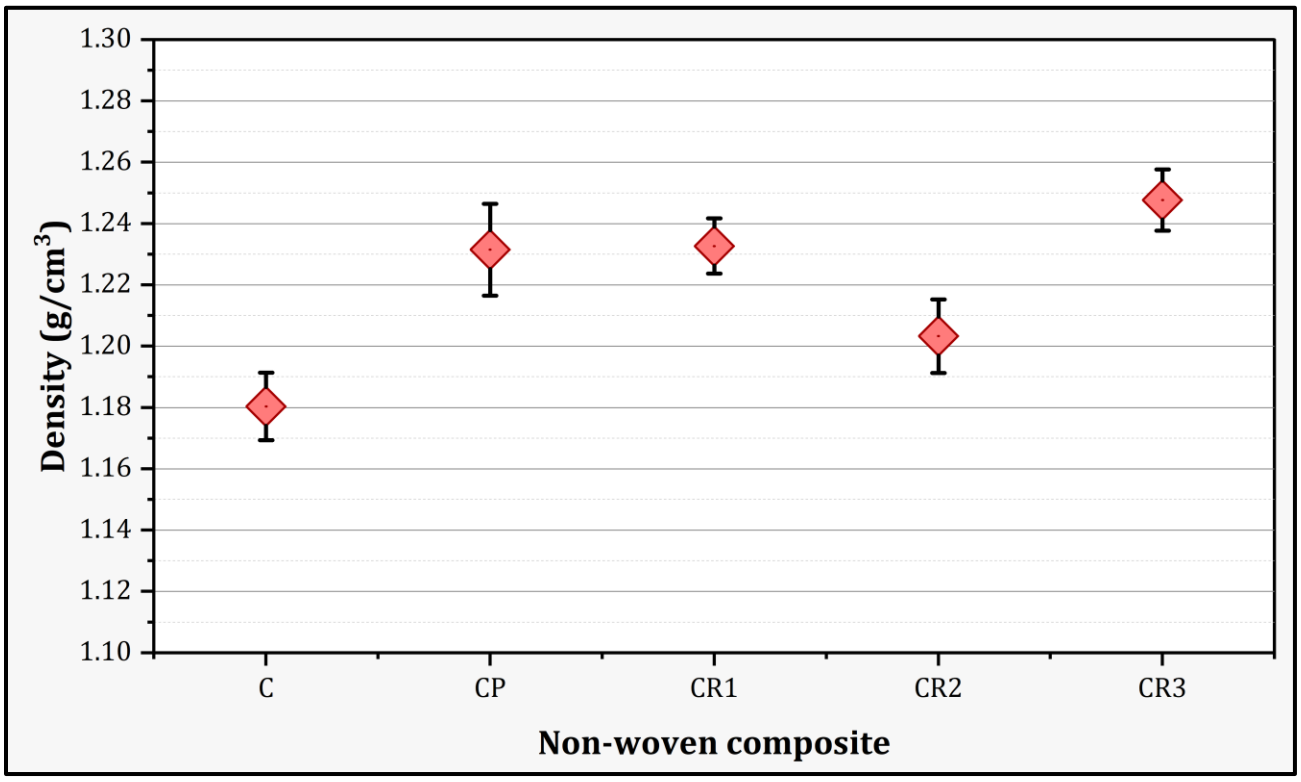


Figure 9. The bulk densities of the unreinforced resin panel and the nonwoven-reinforced composite panels of CP, CR1, CR2, and CR3 were determined using the Archimedes method.

3.2.2. Tensile Properties

The tensile behavior of the unreinforced resin (C) and non-woven-reinforced composite panels of CP, CR1, CR2, and CR3 was evaluated via engineering stress–strain curves obtained under uniaxial loading, with the resulting curves presented in Figure **10** to Figure **14** and the corresponding tensile properties summarized in Table **4**. Sample C was tested only in a single loading configuration (Figure **10**), whereas samples CP, CR1, CR2, and CR3 were each evaluated along the X, Y, and 45° directions (Figure **11** to Figure **14**), corresponding with the anisotropic structure of the non-woven reinforcements. In terms of

maximum tensile load, sample C recorded 460 N in the tested direction. Among the reinforced composites, CR3 exhibited the highest maximum tensile load in all three orientations, reaching 2216 N in the X-direction, 2488 N in the Y-direction, and 2314 N at 45° (Figure **14**). CP showed the second-highest values with 1711 N in X, 2113 N in Y, and 1800 N at 45° (Figure **11**), followed by CR2 with 1273 N in X, 1777 N in Y, and 1449 N at 45° (Figure **13**). CR1 recorded the lowest maximum tensile load among the reinforced samples, at 1189 N in X, 1357 N in Y, and 1273 N at 45° (Figure **12**). Across all reinforced composites, the Y-direction consistently yielded the highest maximum tensile load compared with the X- and 45° directions (Table **4**). Elongation values exhibited a distinct pattern with respect to load-bearing capacity. Sample C exhibited an elongation of 1.9% in its tested direction. CR3 displayed higher elongation than the other reinforced composites, reaching 11.26% in the X-direction, 10.5% in the Y-direction, and 5.12% at 45° (Table **4**). In contrast, CP, CR1, and CR2 exhibited comparatively lower elongation values, ranging from 1.63% to 7.39% across the three directions, with CR1 recording the lowest elongation at 1.33% in X, 1.75% in Y, and 1.63% at 45° (Figure **12**). Tensile toughness values, reflecting the energy absorbed up to failure, showed the largest disparity among the samples. Sample C exhibited a tensile toughness of 996 N in the tested direction. CR3 exhibited the highest tensile toughness across all directions, at 20,927 N in X, 22,395 N in Y, and 9487 N at 45°, representing substantially greater values than those recorded for CP with 4250 N in X, 13,177 N in Y, 10,070 N at 45°, CR2 achieved 1286 N in X, 2038 N in Y, 1532 N at 45°), and CR1 recorded 818 N in X, 1271 N in Y, 1123 N at 45° (Table **4**). CR1 always recorded the lowest tensile toughness among the reinforced composites across all three directions. The modulus of elasticity varied across samples and directions without a uniform trend. Sample C exhibited a modulus of 2217 MPa. Among the reinforced composites, CR1 recorded the highest modulus in the X-direction with 3387 MPa, while CR3 recorded the highest modulus in the Y-direction of 3625 MPa. CP showed relatively consistent modulus values across directions, achieving 3076 in X, 2283 in Y, and 2308 at 45°, whereas CR2 exhibited the lowest

modulus values among the reinforced samples in the X- and Y-directions with 1586 and 2102, respectively (**Table 4**).

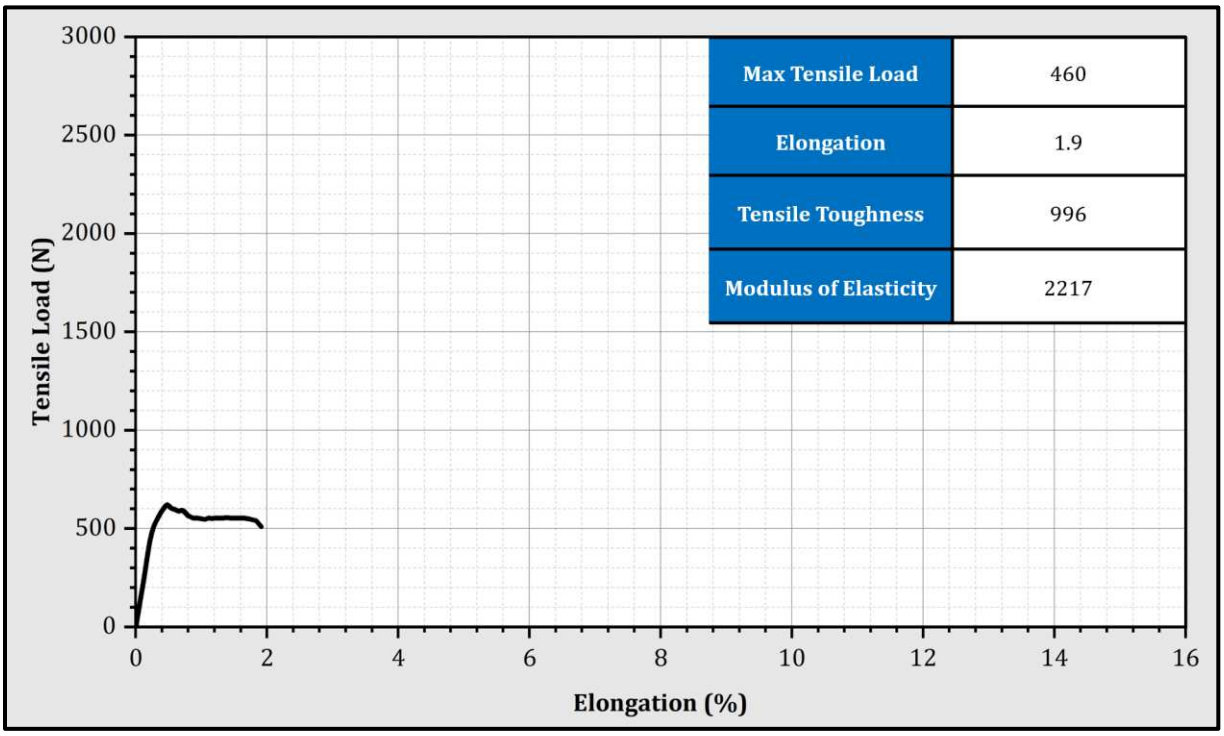
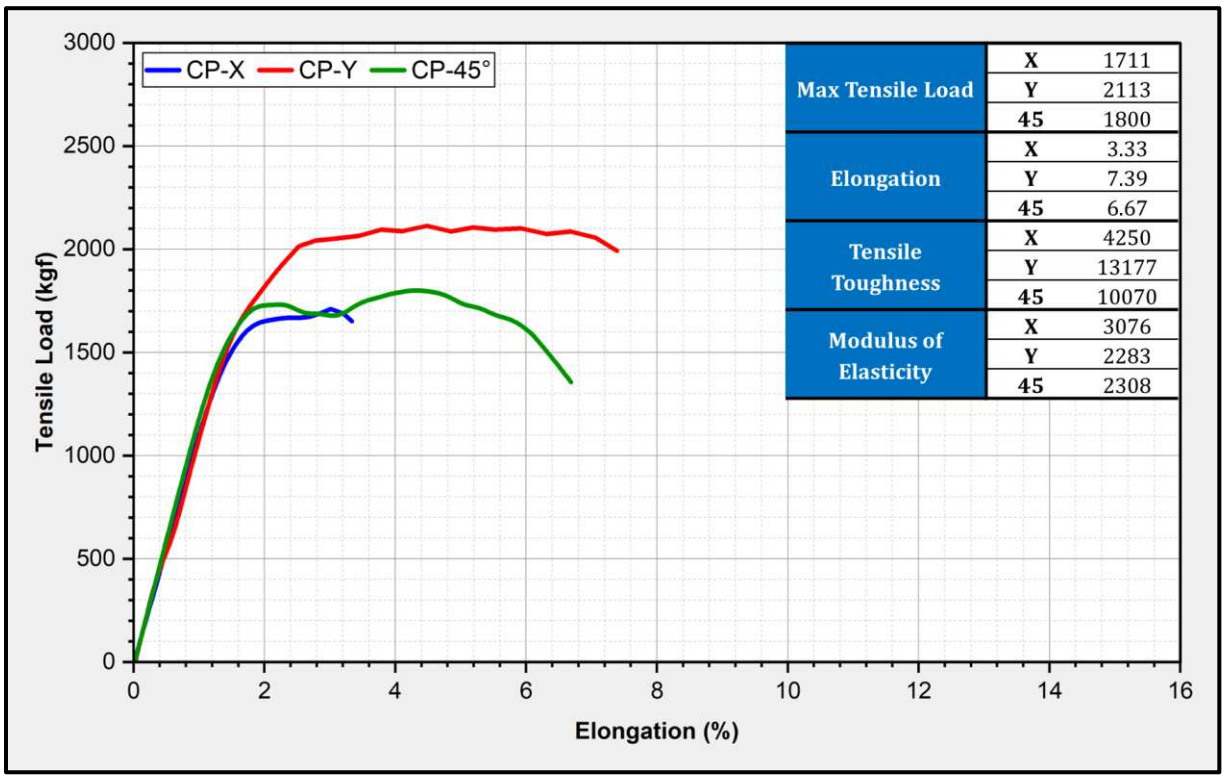
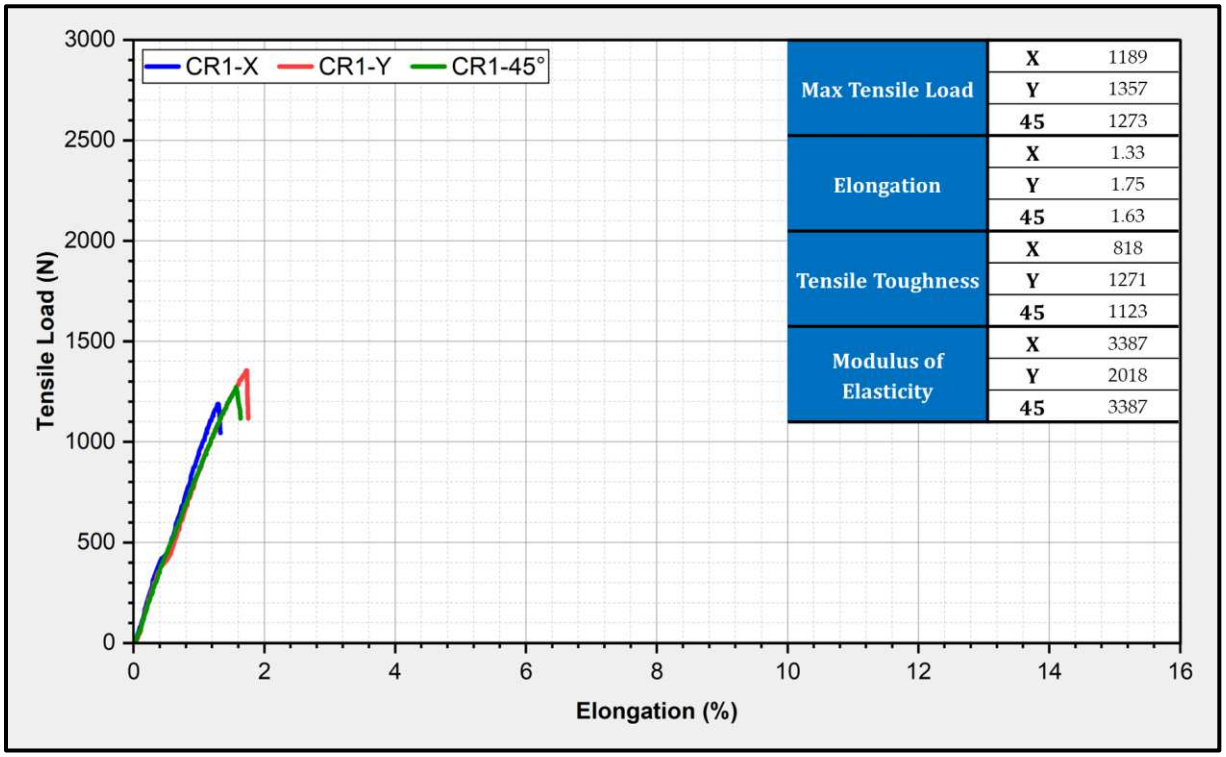


Figure 10. Engineering tensile stress–strain curve and derived tensile properties (maximum load, elongation, toughness, and modulus of elasticity) of the unreinforced resin panel (C).



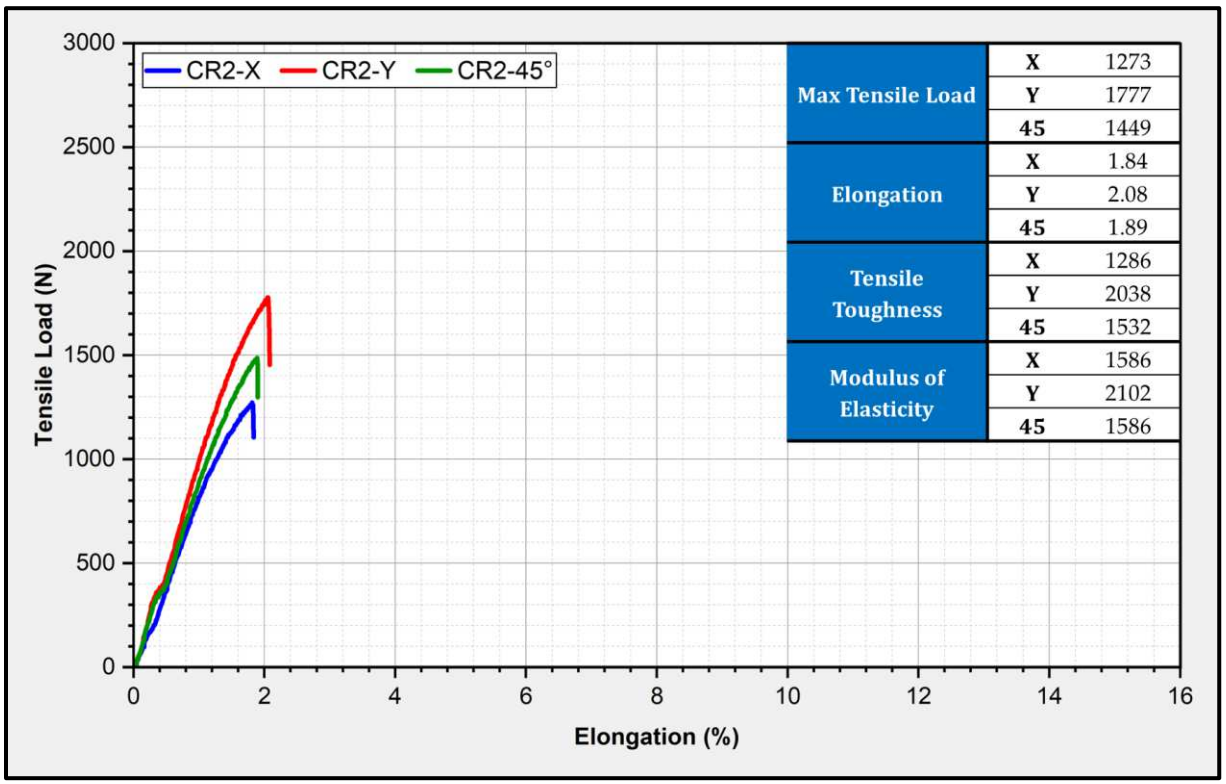
Max Tensile Load	X	1711
	Y	2113
	45	1800
Elongation	X	3.33
	Y	7.39
	45	6.67
Tensile Toughness	X	4250
	Y	13177
	45	10070
Modulus of Elasticity	X	3076
	Y	2283
	45	2308

Figure 11. Engineering tensile stress–strain curves and derived tensile properties of the CP composite panel tested along the X, Y, and 45° directions.



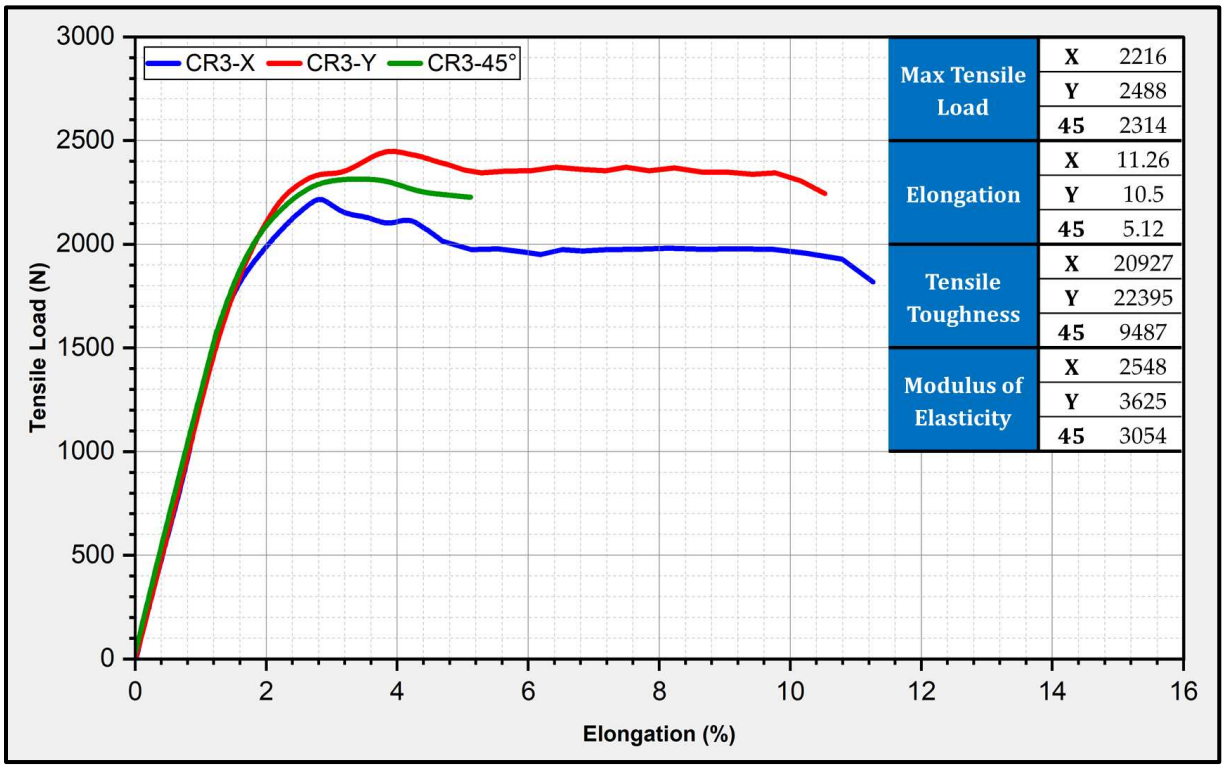
Max Tensile Load	X	1189
	Y	1357
	45	1273
Elongation	X	1.33
	Y	1.75
	45	1.63
Tensile Toughness	X	818
	Y	1271
	45	1123
Modulus of Elasticity	X	3387
	Y	2018
	45	3387

Figure 12. Engineering tensile stress–strain curves and derived tensile properties of the CR1 composite panel tested along the X, Y, and 45° directions.



Max Tensile Load	X	1273
	Y	1777
	45	1449
Elongation	X	1.84
	Y	2.08
	45	1.89
Tensile Toughness	X	1286
	Y	2038
	45	1532
Modulus of Elasticity	X	1586
	Y	2102
	45	1586

Figure 13. Engineering tensile stress–strain curves and the derived tensile properties of the CR2 composite panel tested along the X, Y, and 45°directions.



Max Tensile Load	X	2216
	Y	2488
	45	2314
Elongation	X	11.26
	Y	10.5
	45	5.12
Tensile Toughness	X	20927
	Y	22395
	45	9487
Modulus of Elasticity	X	2548
	Y	3625
	45	3054

Figure 14. Engineering tensile stress–strain curves and derived tensile properties of the CR3 composite panel tested along the X, Y, and 45° directions.

Table 4. Tensile properties of the unreinforced resin panel and non-woven-reinforced composite panels tested along the X, Y, and 45° directions

Tensile Properties	Direction	C	CP	CR1	CR2	CR3
Max Tensile Load (N)	**X**	460	1711	1189	1273	2216
	Y		2113	1357	1777	2488
	45		1800	1273	1449	2314
Elongation (%)	**X**	1.9	3.33	1.33	1.84	11.26
	Y		7.39	1.75	2.08	10.5
	45		6.67	1.63	1.89	5.12
Tensile Toughness (N)	**X**	996	4250	818	1286	20927
	Y		13177	1271	2038	22395
	45		10070	1123	1532	9487
Modulus of Elasticity	**X**	2217	3076	3387 797	1586 806	2548
	Y		2283	2018 961	2102 884	3625
	45		2308	3387 848	1586 987	3054

The fracture surface morphology of the CP and CR3 composite panels following tensile testing was examined by FE-SEM for each loading direction, with observations reported along the X-direction (Figure **15**), the Y-direction (Figure **16**), and the 45°-direction (Figure **17**). Along the X-direction (Figure **15**), the CP fracture surface exhibited fiber/matrix debonding tracks, fiber exposure, void formation associated with fiber pull-out, fiber breakage near the surface of matrix separation, and matrix separation, which was more extensive than in any other sample–direction combination examined in this comparison. In the CR3 sample tested in the X-direction, fiber/matrix debonding tracks were less pronounced than in CP, while fiber exposure was greater than in CP. Void formation associated with fiber pull-out was also observed in CR3, and fiber breakage near the surface of matrix separation was less pronounced than in CP. Matrix separation in CR3 was likewise reduced relative to CP in the X-direction, and the CR3 fracture surface additionally displayed fiber breakage together with fiber elongation. Along the Y-direction (Figure **16**), the CP fracture surface was characterized by fiber breakage near the surface of

matrix separation and by breakage accompanied by fiber elongation. Void content in CP at this orientation was lower than that observed in the corresponding X-direction samples, and matrix separation was likewise reduced relative to the X-direction. The CR3 fracture surface in the Y-direction was dominated by fiber breakage with pronounced fiber elongation covering the bottom surface of the matrix; this elongated-fiber feature was reported as more extensive than the elongated-fiber features observed in the X-direction CP and CR3 samples and in the Y-direction CP sample. Along the 45°-direction (Figure **17**), the fracture surface features attributed to CP consisted mainly of breakage with pronounced fiber elongation covering the bottom surface of the matrix; this feature was described as more extensive than in the X-direction CP and CR3 samples and in the Y-direction CP sample, but less extensive than in the Y-direction CR3 sample, with the overall morphology at 45° reported as broadly resembling that of the X-direction CP sample. The CR3 fracture surface at 45° exhibited fiber breakage near the surface of matrix separation, breakage accompanied by fiber elongation, a void content lower than that of the X-direction samples, and matrix separation. It can be concluded that the fracture-surface observations in Figure **15**, Figure **16**, and Figure **17** indicate that fiber/matrix debonding tracks and matrix separation were most extensive in the X-direction for both CP and CR3, with CP consistently showing greater debonding and matrix separation than CR3 in this orientation. In contrast, fiber breakage accompanied by fiber elongation emerged as the predominant fracture feature in the Y- and 45°-direction samples for both CP and CR3, with the Y-direction CR3 sample exhibiting the most extensive fiber elongation among all sample–direction combinations reported. Void formation was present across all three directions for both samples, but was comparatively reduced in the Y- and 45°-directions relative to the X-direction.

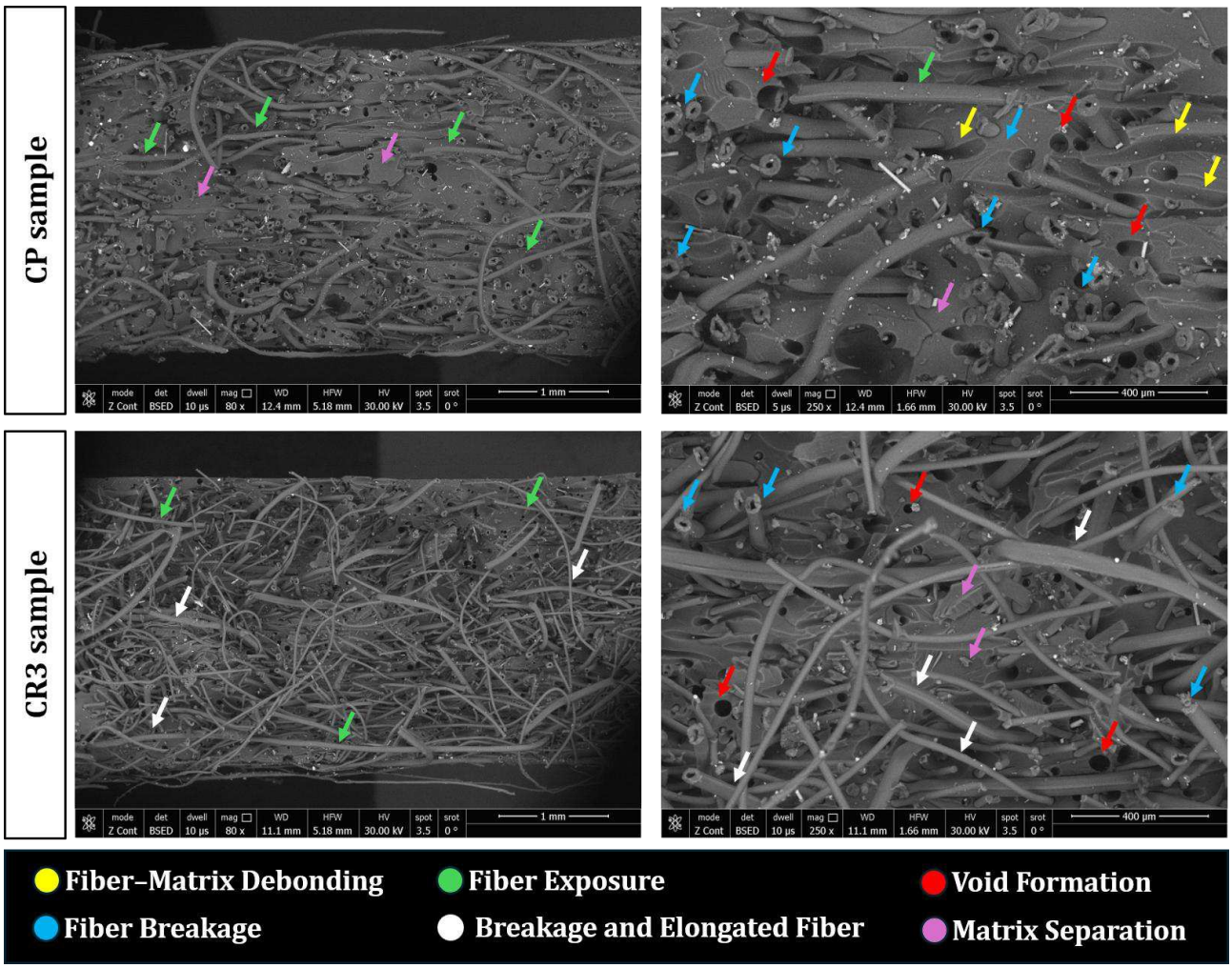


Figure 15. FE-SEM of the fracture surface morphology of the CP and CR3 composite panels tested along the X direction.

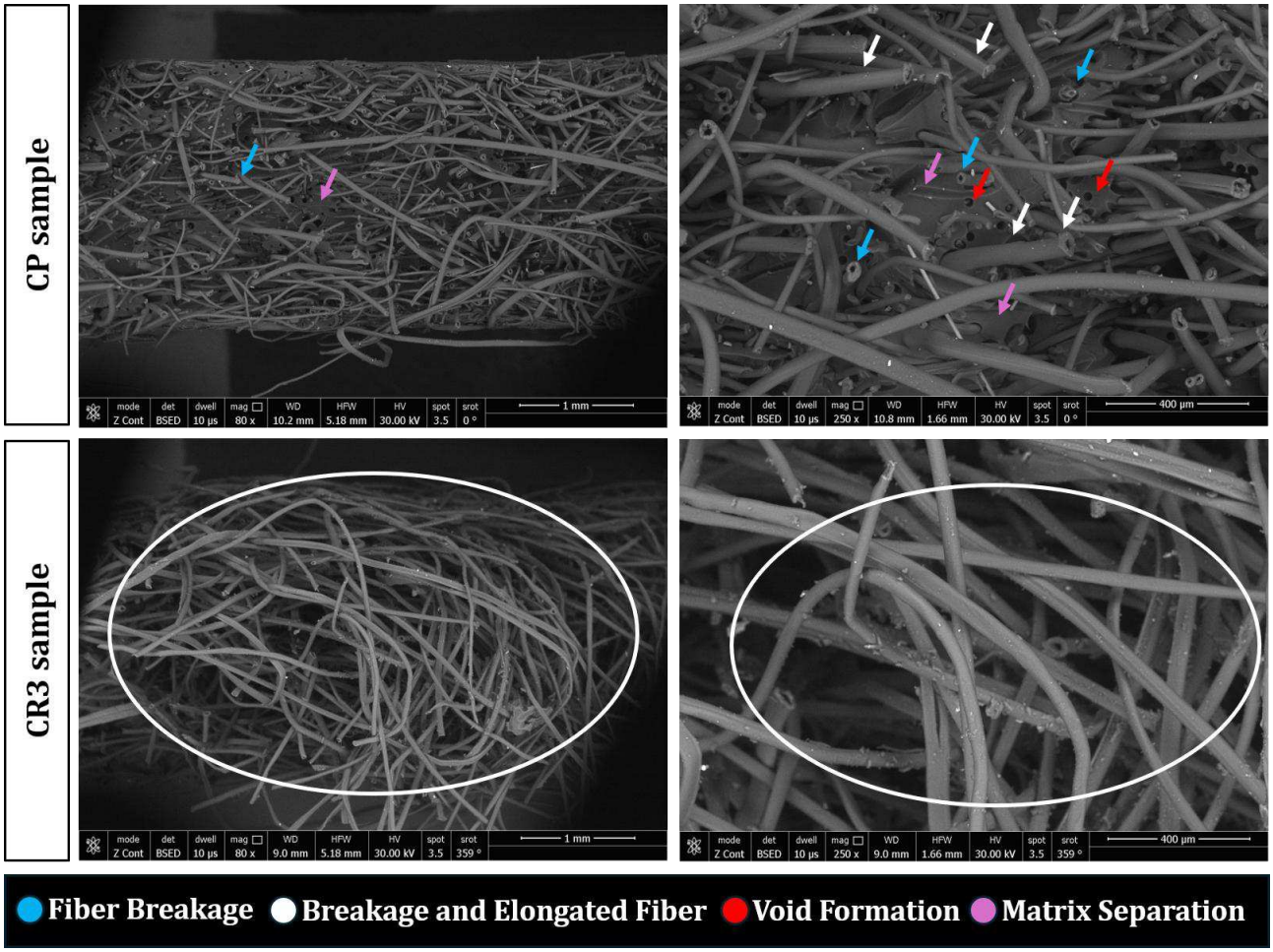


Figure 16. FE-SEM images of the fracture surface morphologies of the CP and CR3 composite panels tested along the Y-direction.

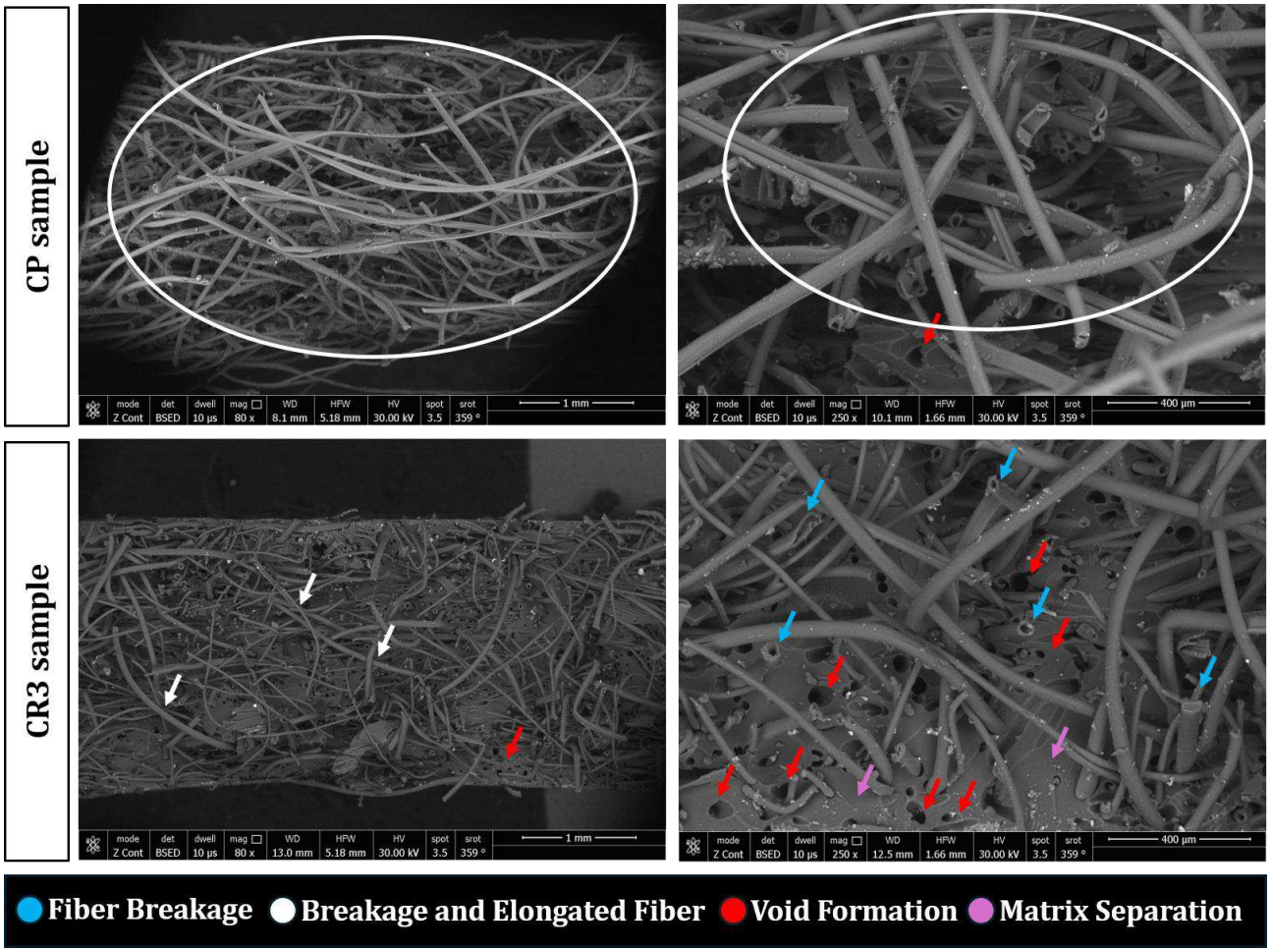


Figure 17. FE-SEM images of the fracture surface morphology of the CP and CR3 composite panels tested along the 45°direction.

3.2.3. Tribological Wear Behavior

The volumetric wear loss of the unreinforced resin (C) and nonwoven-reinforced composite panels of CP, CR1, CR2, and CR3 were evaluated under dry sliding conditions at applied loads of 15 N, 25 N, and 35 N, and the results are presented in Figure **18**. Across all five sample groups, the volumetric wear loss increased progressively with increasing applied load, indicating a consistent load-dependent wear trend. At the lowest applied load of 15 N, sample C exhibited the highest volumetric wear loss among all groups, at 0.8457 ± 0.0471 ($\times 10^{-}$ cm³), followed by CR1 at 0.6489 0.6489 ± 0.0395, CP at ± 0.0383, CR3 at 0.3205 ± 0.0216, and CR2, which recorded the lowest wear loss at 0.2162±0.0299, as shown in Figure **18**. At 25 N, the same relative ordering was largely maintained, with sample C again showing the highest volumetric wear loss of 1.6031 ± 0.0513, followed by CR1 at 1.0545 ± 0.0527, CP at 0.5758 ± 0.0318,

CR3 at 0.4808 ± 0.0240, and CR2 remaining the lowest at 0.4155 ± 0.0208. At the highest applied load of 35 N, sample C exhibited the greatest volumetric wear loss overall, at 1.8507 ± 0.0617, followed by CR1 at 1.2979 ± 0.0779, CP at 1.1163 ± 0.0670, CR3 at 0.7732 ± 0.0464, and CR2 again recording the lowest value, at 0.6648 ± 0.0399 (Figure **18**). Across all three loading conditions, sample C consistently exhibited the highest volumetric wear loss, whereas CR2 consistently exhibited the lowest, indicating a reproducible ranking pattern across the tested load range. CR1 consistently recorded a higher wear loss than CP and CR3 at all three loads, whereas the relative positions of CP and CR3 varied slightly with load: CR3 exhibited a lower wear loss than CP at 15 N and 25 N, but at 35 N, CR3 achieved 0.7732, which remained lower than CP with 1.1163, maintaining the same relative order, as shown in Figure **18**.

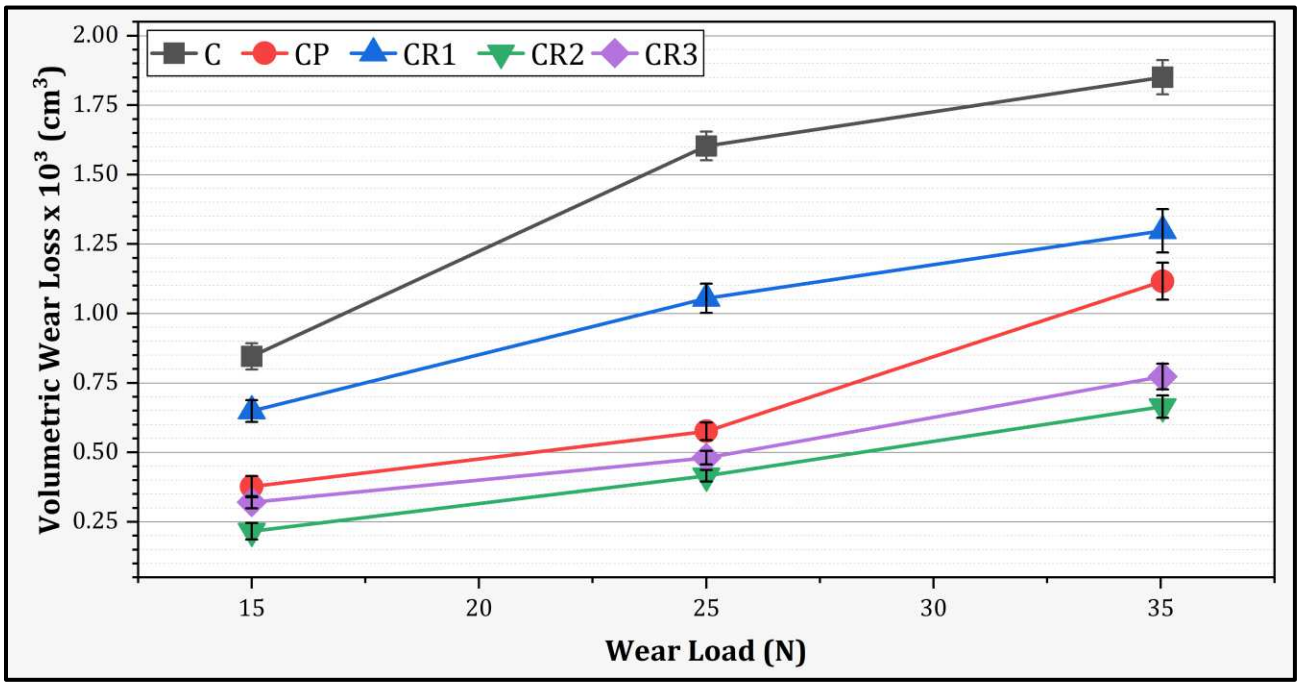


Figure 18. Volumetric wear loss of the unreinforced resin panel and non-woven-reinforced composite panels as a function of applied load of 15, 25, and 35 N under dry sliding tests.

The width of the wear track developed during dry sliding tests of the unreinforced resin panel of C and the non-woven-reinforced composite panels of CP, CR1, CR2, and CR3 was evaluated as a function of applied loads of 15 N, 25 N, and 35 N, as presented in Figure **19**. Across all five sample groups, the wear track width increased progressively with increasing applied load, indicating a consistent load-dependent widening trend. At 15 N, sample C exhibited the widest wear track, at 1.615, followed by CR1 at 1.387,

CP at 1.175, CR2 at 1.1341, and CR3, which recorded the narrowest track at 1.094, as shown in Figure **19**. At 25 N, sample C again showed the widest track, at 1.728, followed by CR1 at 1.497, CP at 1.267, CR3 at 1.183, and CR2 at 1.153. At the highest applied load of 35 N, sample C exhibited the widest wear track overall, at 1.938, followed by CR1 at 1.715, CP at 1.431, CR3 at 1.215, and CR2 at 1.194, as presented in Figure **19**. Sample C consistently produced the widest wear track and CR1 the second-widest across all three applied loads, while CP occupied an intermediate position at each load level. In relative terms, the wear track width increased from 15 N to 35 N by approximately 20.0% for C, 21.8% for CP, and 23.65% for CR1. Notably, the relative ranking of CR2 and CR3 was not consistent across the tested load range: CR3 recorded the narrowest wear track at 15 N of 1.094 versus 1.1341 for CR2, whereas CR2 recorded the narrowest track at both 25 N with 1.153 versus 1.183 for CR3 and 35 N with 1.194 for CR2 versus 1.215 for CR3. Over the same load range, the wear track width increased by approximately 5.35% for CR2 and 11.06% for CR3, indicating that these two samples exhibited a comparatively smaller relative widening of the wear track than C, CP, and CR1.

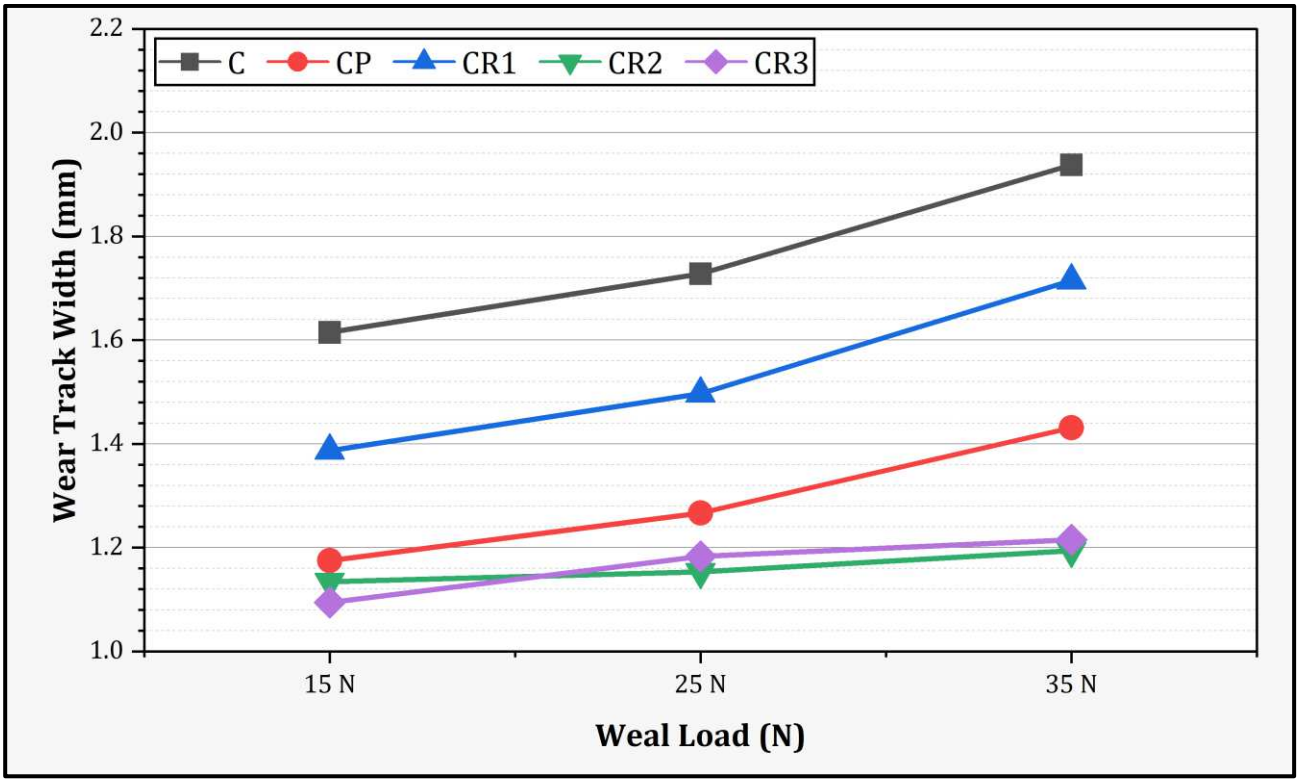


Figure 19. Width of wear track developed during dry sliding tests of the unreinforced resin panel and the nonwoven-reinforced composite panels as a function of applied load of 15, 25, and 35 N.

The worn surface morphology of the CP and CR3 composite panels after dry sliding wear testing at applied loads of 15 N and 35 N was examined by SEM, with micrographs presented for CP in Figure **20** and for CR3 in Figure **21**. At 15 N, the CP-worn surface exhibited plastic-deformed regions, debris, and interfacial bonding cracks. At 35 N, the CP-worn surface again showed plastic-deformed regions and debris, with interfacial bonding cracks reported as more extensive than those at 15 N. At 15 N, the CR3-worn surface exhibited clear plastic-deformed regions accompanied by small and small debris, with no interfacial bonding cracks observed. At 35 N, the CR3-worn surface likewise showed clear plastic-deformed regions, with debris reported as greater in extent than that at 15 N, while no interfacial bonding cracks were observed at either load level. It can be remarked that the Figure **21** observations indicate that plastic deformation was present on the worn surfaces of both CP and CR3 at both applied loads, and that debris accumulation increased with increasing load for both samples. Interfacial bonding cracks were observed on the CP-worn surface at both 15 N and 35 N, increasing in extent between the two load levels, whereas no interfacial bonding cracks were reported for CR3 at either load level.

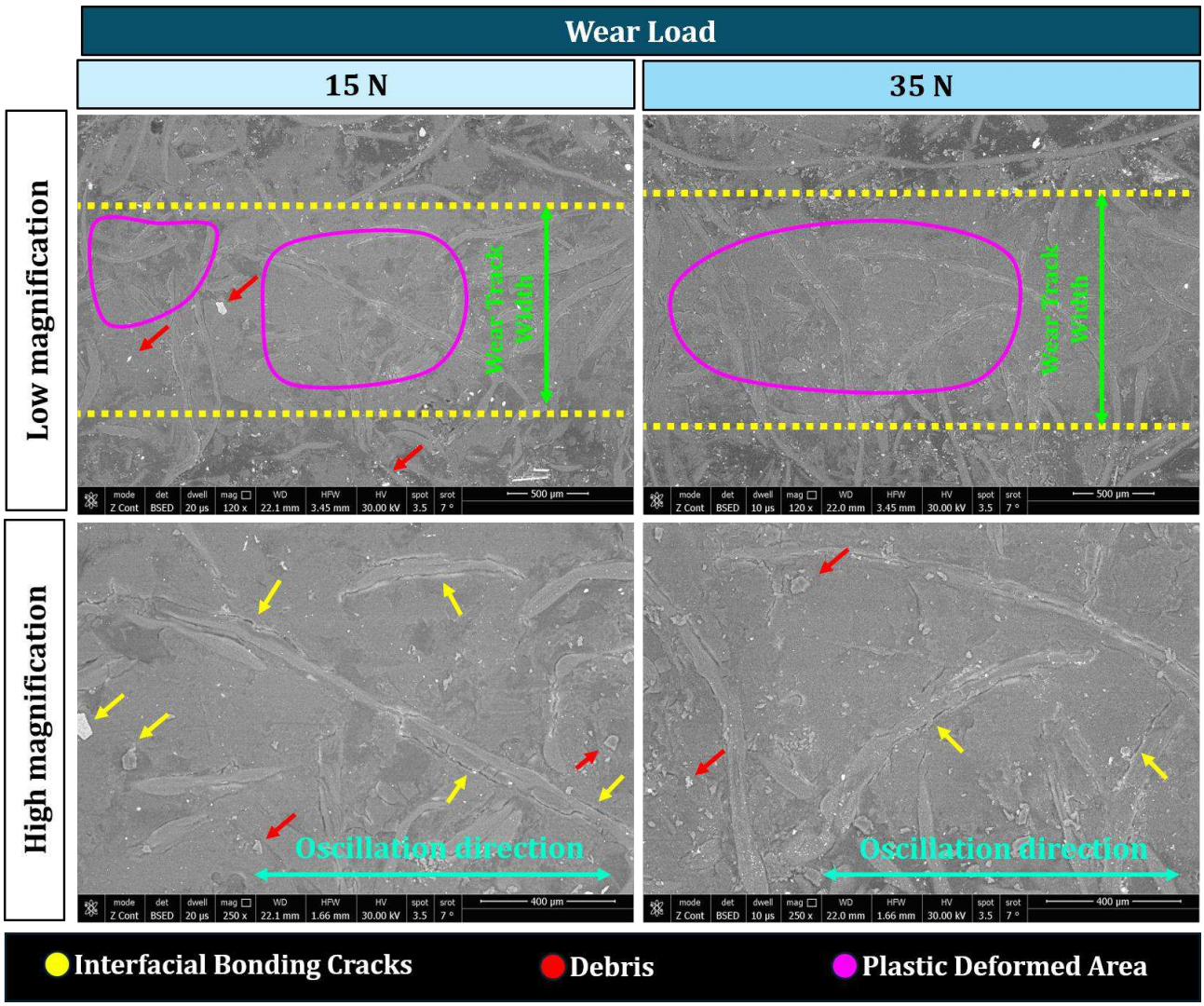


Figure 20. SEM images of the nonwoven-reinforced composite surface panels of the CP sample after the dry sliding wear test at wear loads of 15 and 35 N.

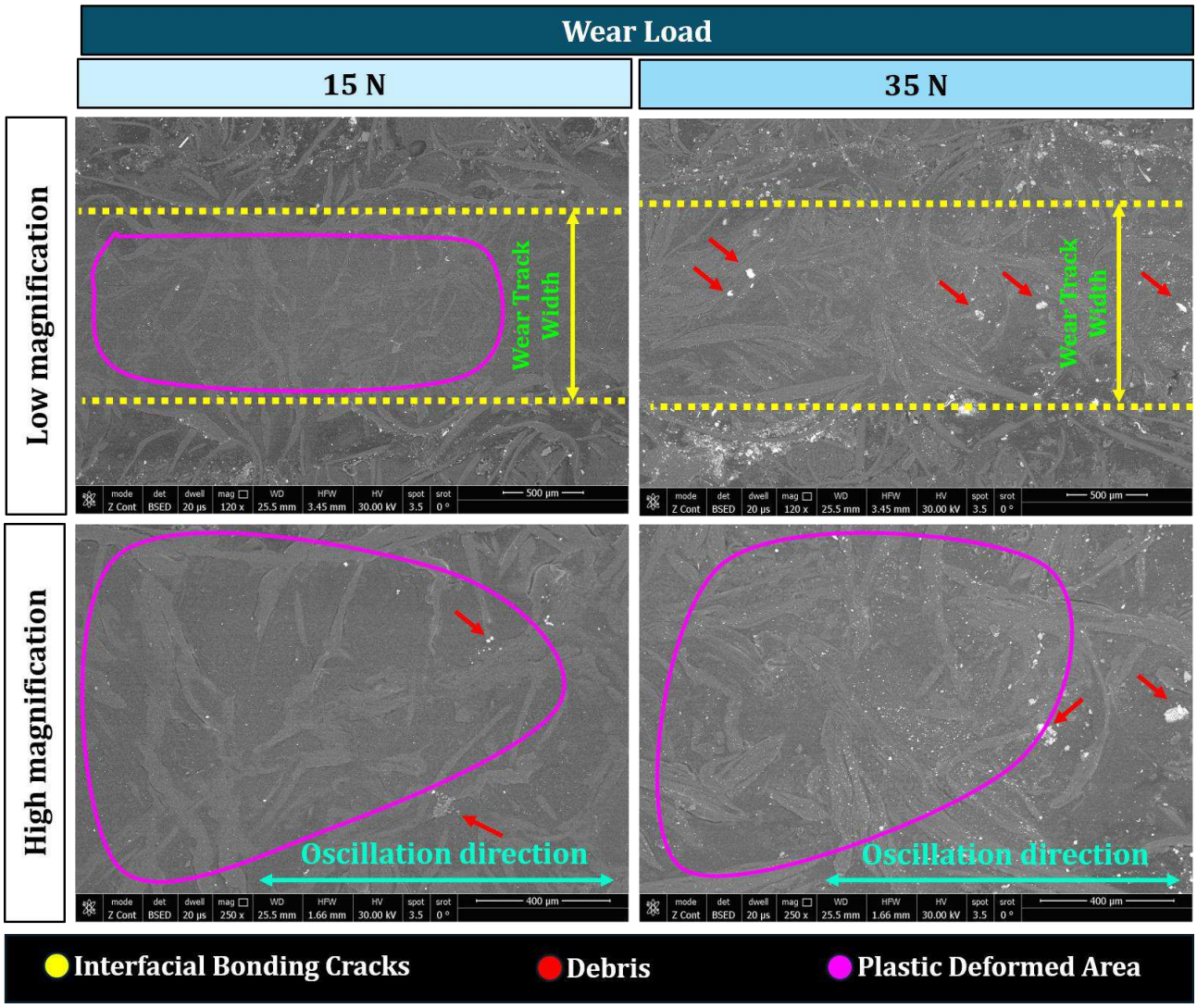


Figure 21. Worn surface SEM image of nonwoven-reinforced composite surface panels of the CR3 sample after dry sliding wear test at wear loads of 15 and 35 N.

3.2.4. Water Absorption and Thickness Swelling

The water absorption behavior of the unreinforced resin and non-woven-reinforced composite panels of CP, CR1, CR2, and CR3 were assessed following immersion periods of 2 h, 24 h, 48 h, 72 h, and 10 days, with the results presented in Figure **22**. During the initial 2-hour immersion interval, sample CR1 exhibited the highest water absorption among all groups, at 0.124 ± 0.0062%, followed by sample C at 0.068 ± 0.003%, CR3 at 0.041 ± 0.002%, and CR2 at 0.033 ± 0.002%. Sample CP recorded the lowest water absorption at this interval, at 0.01±0.001%. At 24 hours, water absorption increased across all sample groups relative to the 2-hour reading. CR1 again exhibited the highest value, at 0.813 ± 0.041%, followed by CP at 0.316 ± 0.016%, C at 0.215 ± 0.0108%, CR3 at 0.301 ± 0.015%, and CR2 at 0.255 ±

0.013% (Figure **22**). At the 48-hour interval, absorption values for all sample groups decreased relative to their respective 24-hour readings: C fell to 0.1 ± 0.005%, CP to 0.271 ± 0.0136%, CR1 to 0.539 ± 0.026%, CR2 to 0.181 ± 0.001%, and CR3 to 0.245 ± 0.012%. Absorption values then increased again at 72 hours for all samples, exceeding both the 24-hour and 48-hour readings: C reached 0.36±0.018%, CP reached 0.69±0.0345%, CR1 reached 1.52±0.076%, CR2 reached 0.42±0.021%, and CR3 reached 0.54±0.027%. At this interval, CR1 exhibited the highest water absorption among all groups, exceeding CP, the next-highest sample, by more than a factor of two. After 10 days of immersion, water absorption increased substantially across all sample groups relative to the 72-hour readings. CR1 recorded the highest overall value, at 2.98635±0.149%, followed by C at 2.66131±0.133%, CR2 at 1.31139±0.065%, CR3 at 0.95394±0.048%, and CP at 1.01039±0.051%, as presented in Figure **22**. At this final measured interval, CR1 exhibited the highest water absorption among all five sample groups, while CR3 recorded the lowest value among the non-woven-reinforced composites.

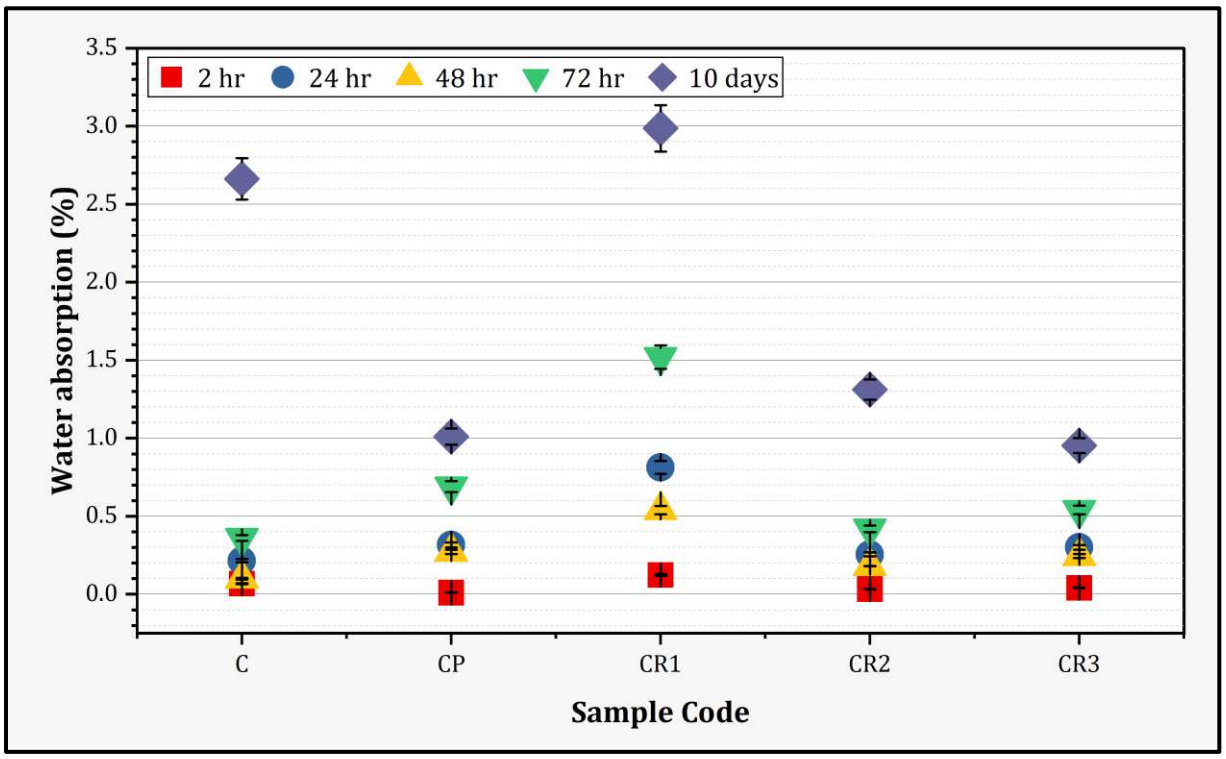


Figure 22. Water absorption of the unreinforced resin panel and non-woven-reinforced composite panels after 2 h, 24 h, 48 h, 72 h, and 10 days of immersion in distilled water.

The thickness swelling behavior of the unreinforced resin (C) and the non-woven-reinforced composite panels of CP, CR1, CR2, and CR3 was assessed following immersion periods of 2 h, 24 h, 48 h, 72 h, and 10 days, with the results presented in Figure **23**. A notable feature of this dataset is that all four reinforced composites of CP, CR1, CR2, and CR3 exhibited negative thickness swelling values at most immersion intervals, whereas sample C exhibited positive values throughout the entire immersion period. At the 2-hour immersion interval, sample C exhibited a thickness swelling of 4.15 ± 0.207%, the highest value recorded among all groups at this time point. In contrast, CR1 exhibited the most negative value, at −7.92 ± 0.396%, followed by CR3 at −1.96±0.098%, CP at −2.73 ± 0.1365%, and CR2 at −1.48±0.074% (Figure **23**). At 24 hours, sample C showed a reduced thickness swelling of 1.19 ± 0.0595% relative to its 2-hour value. Among the reinforced composites, CR1 remained the most negative, at -6.64 ± 0.332%, while CR3 was the only reinforced sample to record a positive value in this interval, at 0.69 ± 0.0345%. CP and CR2 recorded −1.88 ± 0.094% and −1.46 ± 0.073%, respectively. At the 48-hour interval, sample C increased to 3.2 ± 0.16%, exceeding its 24-hour value. CR1 again exhibited the most negative reading, at −6.92 ± 0.346%, matching its subsequent 72-hour value exactly. CR3 shifted back to a negative value at this interval, at −0.07 ± 0.004%, the value closest to zero among all reinforced samples across the entire immersion series. CP and CR2 recorded −2.31 ± 0.115% and −2.02 ± 0.101%, respectively. At 72 hours, sample C decreased to 1.96 ± 0.098%. CR1 recorded −6.92±0.346%, identical to its 48-hour value. CR3 returned to a positive value, at 0.89 ± 0.0445%, the highest value recorded among the reinforced composites at this time point. CP and CR2 recorded −1.52 ± 0.076% and −1.6 ± 0.081%, respectively, as shown in Figure **23**. After 10 days of immersion, the trend for all sample groups reversed relative to the earlier intervals, with every sample recording a positive thickness swelling value. CR1 exhibited the highest value among all groups, at 2.28119 ± 0.114%, followed by CR3 at 0.828 ± 0.041%, C at 0.05722 ± 0.003%, CR2 at 0.072 ± 0.003%, and CP recording the lowest value, at 0.03681 ± 0.002%.

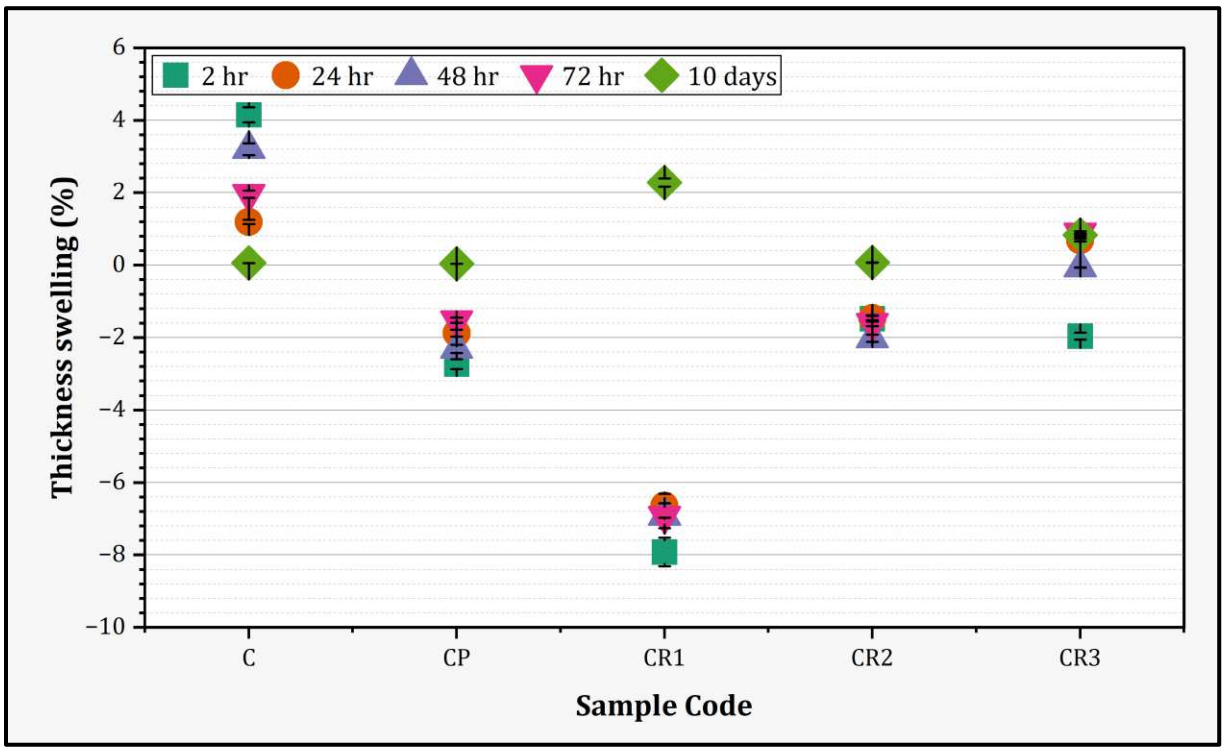


Figure 23. Thickness swelling (%) of the unreinforced resin panel and non-woven-reinforced composite panels after 2, 24 h, 48 h, 72 h, and 10 days of immersion in distilled water.

The surface morphology of the CP and CR3 composite panels following immersion in distilled water for 0 h, 72 h, and 10 days was examined by SEM, with representative micrographs presented in Figure **24**. At the 0 h immersion interval (prior to water exposure), both CP and CR3 exhibited comparable surface characteristics, with smoother matrix surfaces and bonded fibers observed for both samples, as shown in Figure **24**. No distinguishing differences were observed between CP and CR3 at this initial time point. At the 72 h immersion interval, the CP surface showed a reduced degree of smooth matrix surface coverage relative to the 0 h condition, described as "some smoother matrix surfaces," together with the emergence of surface roughening, voids, and partial fiber exposure. The CR3 surface at 72 h likewise displayed surface roughening, voids, and partial fiber exposure, but each of these features was reported as less pronounced than in CP: CR3 retained a greater extent of smoother matrix surface coverage than CP, exhibited surface roughening to a lesser degree than CP, and showed less partial fiber exposure than CP at the same immersion interval. At the 10-day immersion interval, the CP surface exhibited a marked progression in surface degradation, characterized by harsh surface roughening, severe fiber exposure,

interfacial bonding features, and voids. In contrast, the CR3 surface at 10 days showed surface roughening reported as less severe than that of CP, together with partial fiber exposure, voids, and the continued presence of some smoother matrix surface regions. It can be remarked that in Figure **24** observations indicate a progressive, time-dependent increase in surface roughening, void formation, and fiber exposure for both CP and CR3 across the 0 h to 10-day immersion series, with these degradation features consistently reported as less extensive in CR3 than in CP at both the 72 h and 10-day intervals.

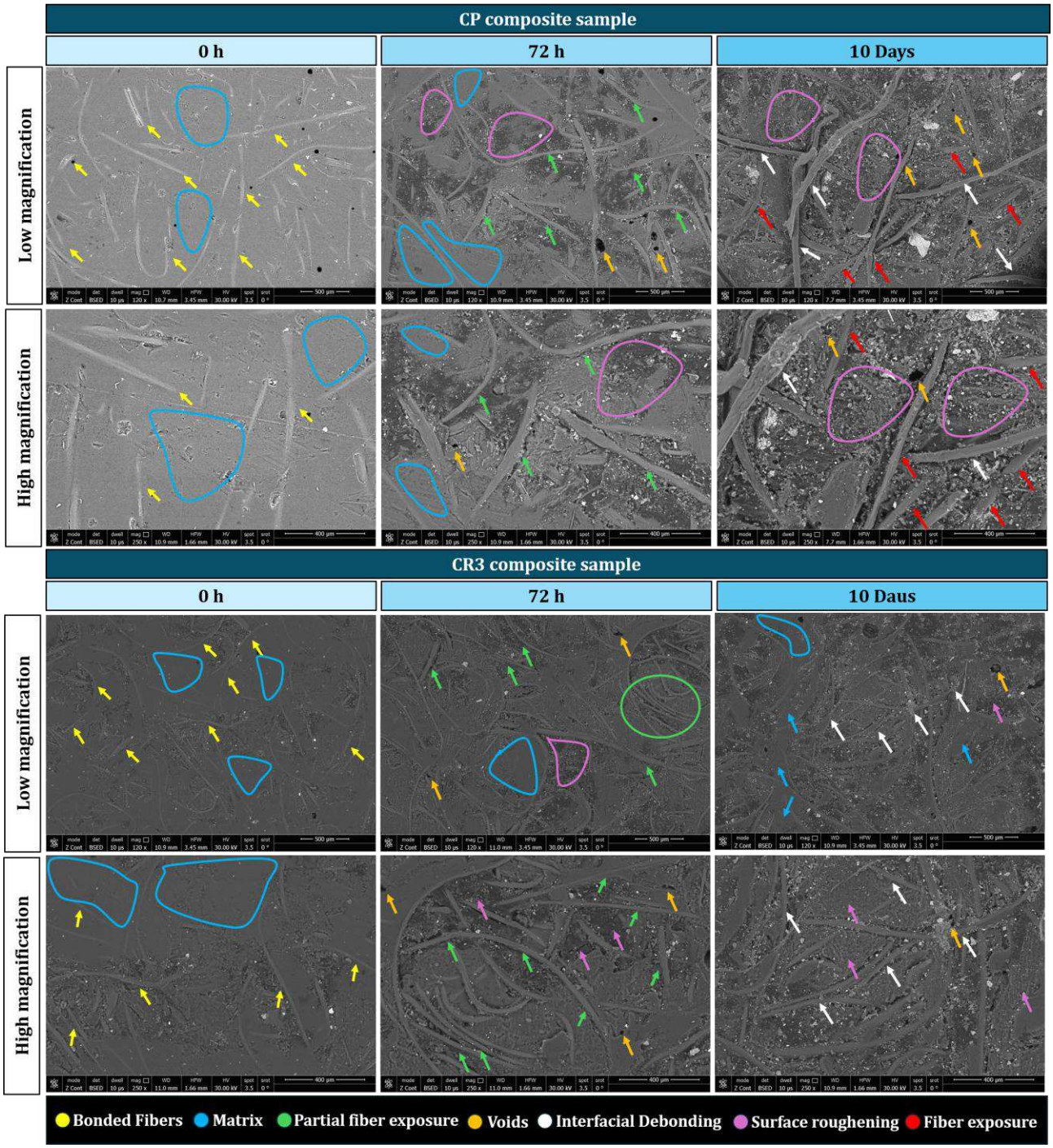


Figure 24. SEM images of non-woven-reinforced composite surface panels of CP and Cr3 samples after 0, 72 h, and 10 days of immersion in distilled water.

4. Discussion

The tensile response of the reinforced panels cannot be interpreted without consideration of the composition and morphological base described in Sections 3.2.1 and 3.2.2. Because the fiber-to-resin mass ratio varied only slightly across CP, CR1, CR2, and CR3, ranging from 29.7% to 33.9% fiber

content, as shown in Table **3**, the significant variations observed in maximum tensile load, elongation, and toughness, most notably the several-fold advantage of CR3 over CR1, cannot be attributed to differences in reinforcement loading fraction and must instead reflect intrinsic differences in fiber source, bonding structure, and interfacial quality inherited from the precursor non-woven matrices. This inference is aligned with the broader previous work by Papán et al. [17] and Monti et al. [15] on recycled poly(ethylene terephthalate) (PET)-based reinforcements, where composite performance is governed less by nominal fiber content than by the processing history and molecular properties of the recycled feedstock; hybrid composites incorporating recycled PET have likewise shown that mechanical performance depends strongly on the specific consolidation and bonding process rather than on fiber mass fraction alone [17–18]. Because CR3 was derived from PET-bottle-sourced fibers combined with thermally bonded sheath-core binder filaments, its superior load-bearing capacity and toughness across all three testing orientations align with reports that the impact and tensile performance of PET-reinforced systems can approach or exceed that of virgin-fiber composites when interfacial bonding is correctly engineered. This relationship between feedstock origin and mechanical performance frames the subsequent directional and fractographic findings not as isolated observations but as consequences of a single underlying structural cause: the fiber-network architecture inherited from the non-woven precursor.

The composite-level tensile hierarchy presented in Section 3.2.2, CR3 > CP > CR2 > CR1 in terms of maximum tensile load, elongation, and toughness, is not an emergent property of the consolidation process but a direct carry-over of the uniaxial load-bearing hierarchy already documented for the precursor nonwoven fabrics in Section 3.1. In the Y-direction strip tensile tests, the raw fabrics ranked R3 (1701.93 N) > P (868.93 N) > R2 (124.13 N) > R1 (9.8–12.2 N), and the grab tensile tests reproduced this identical ordering (R3:1685.60 N; P: 1215.2 N; R2:163.33 N; R1:11.1 N). This is the same rank order subsequently observed for the corresponding composites across all three testing directions in Figure **10**, Figure **11**, Figure **12**, Figure **13**, and Figure **14**, indicating that the fiber-network strength obtained

from the dry preform, rather than any property introduced during resin impregnation and compression consolidation, is the primary determinant of composite tensile capacity. This agreement is consistent with reports that the mechanical properties of non-woven-reinforced composites are directly related to those of the dry non-woven reinforcement, since resin consolidation transmits rather than overrides the load-bearing architecture set at the fabric stage [13].

The fracture-surface evidence in Figure **15**, Figure **16**, and Figure **17** provides a mechanical link between this fabric-level strength hierarchy and the composite-level tensile outcomes for the two directly compared samples, CP and CR3. At the fabric level, Section 3.1 reported that P exhibited the highest displacement at break failure (5.07 ± 0.26 mm) among all precursors, denoting considerable deformation capacity before breaking, whereas R3 achieved the highest bursting strength (2613.33 ± 130.67 N) and highest puncture resistance (944.07 ± 47.2 N), denoting a more robust, tightly interlocked fiber network with less reliance on large-scale deformation to resist failure. This distinction reappears almost unchanged in the tensile fracture morphology of the corresponding composites: in the X-direction, the CP fracture surface exhibited the most extensive fiber/matrix debonding tracks and matrix separation of any sample–direction combination examined, consistent with a fiber network (P) that historically failed through progressive multiaxial deformation rather than abrupt fiber engagement. By contrast, CR3 in the same X-direction showed markedly reduced debonding and matrix separation relative to CP, together with greater fiber exposure and evidence of fiber breakage with elongation, a fractographic signature consistent with the tightly bonded, high-puncture-resistance R3 fiber network resisting interfacial slippage and instead transferring load until localized fiber fracture. This concordance indicates that the debonding-versus-breakage failure balance visible in FE-SEM is not a matrix-driven artifact of the resin but a direct structural inheritance from the bursting- and puncture-resistance characteristics already differentiating P from R3 in Section 3.1.

The directional anisotropy of both the tensile properties and fracture morphology further reinforces this fabric-to-composite continuity. Section 3.1 established that P and R3 both exhibited higher strip and grab

tensile strength in the Y-direction than in the X-direction, attributed to preferential fiber orientation along the machine direction introduced during needle punching. This same directional bias persists in the composite maximum tensile load data, where the Y-direction consistently yielded the highest values for CP (Figure **11**) and CR3 alike (Figure **14**), and it is mirrored again in the fracture surfaces: the X-direction, corresponding to the cross-machine, comparatively lower-strength orientation at both the fabric and composite level, showed the greatest debonding and matrix separation for both CP and CR3, whereas the Y- and 45°-direction surfaces, corresponding to the higher-strength orientations, were instead dominated by fiber breakage accompanied by pronounced fiber elongation, with the Y-direction CR3 sample showing the most extensive elongated-fiber coverage among all sample–direction combinations examined. This alignment between the weaker cross-direction favoring interfacial debonding and the stronger machine-direction favoring fiber breakage indicates that the anisotropic fiber orientation imposed during non-woven manufacture governs not only the magnitude of composite tensile properties but also the specific micromechanical failure pathway observed post-fracture, a relationship consistent with broader evidence that manufacturing-stage fiber architecture in non-woven-reinforced composites conditions both the macroscopic mechanical response and the resulting fracture mechanism. The elongation behavior, however, marks a point where fabric-level and composite-level trends do not perfectly align, and this divergence is itself informative when read alongside the fracture morphology. At the fabric level, Y-direction strip elongation ranked R3 (98%) > P (88.33%) > R1 (46%) > R2 (34%), yet at the composite level, CR2 (2.08% in Y) exceeded CR1 (1.75% in Y), reversing the R1–R2 order seen in the dry fabric. The observed effect is due to the surrounding cured resin, which differentially constrains fiber mobility based on each precursor's porosity and bonding density. This interaction is not captured by dry-fabric extensibility measurements alone. This partial decoupling, occurring specifically for strain-based properties while strength- and toughness-based rankings remain fully preserved from fabric to composite, indicates that resin confinement introduces a resin-dependent modifier layered on top of the otherwise dominant fabric-inherited mechanical hierarchy.

The tribological ranking observed under dry sliding conditions, in which the unreinforced resin (C) consistently exhibited the greatest volumetric wear loss and widest wear track across all three applied loads of 15, 25, and 35 N, while CR2 consistently showed the lowest wear loss, situates the wear behavior of these panels within the well-documented principle that fibrous reinforcement redistributes and mitigates contact stresses at the sliding interface, thereby reducing volumetric material removal relative to the unreinforced matrix. This mechanism has been repeatedly confirmed in natural- and recycled-fiber-reinforced polymer systems subjected to pin-on-disc or pin-on-flat sliding wear [19-21]. However, the fact that CR2 outperformed CR3 tribologically despite CR3's markedly superior tensile toughness and maximum load indicates that the bulk tensile performance and sliding wear resistance are governed by partially decoupled structural attributes in this system; this decoupling parallels observations in fiber-reinforced epoxy hybrids, where wear resistance has been shown to depend more strongly on surface-level fiber packing density, layer architecture, and local hardness at the contact interface than on bulk toughness metrics derived from tensile testing. The load-dependent widening of the wear track alongside progressively greater debris accumulation on both CP (Figure **20**) and CR3 (Figure **21**) worn surfaces is consistent with a transition toward more severe abrasive/adhesive wear at higher contact loads, a pattern similarly reported for banana- and jute-fiber-reinforced composites under increasing normal load, where interfacial bonding-crack density and debris generation both intensify as the applied load increases. Notably, the presence of interfacial bonding cracks exclusively on the CP-worn surface and their complete absence on CR3 at both 15 N and 35 N reinforce the interfacial-quality argument developed from the tensile fractography: the same fiber–matrix coupling that limited debonding under uniaxial tensile loading in CR3 appears to similarly restrain crack initiation at the sliding contact interface, suggesting that interfacial adhesion, rather than reinforcement type per se, is the common structural variable linking tensile fracture behavior and tribological durability across these panels.

The water absorption (Figure **22**), thickness swelling (Figure **23**), and SEM surface (Figure **24**) evidence together indicate that CP and CR3 diverge progressively in moisture-driven surface degradation despite

starting from indistinguishable conditions. At 0 h, both panels displayed smoother matrix surfaces with well-bonded fibers, and no distinguishing feature separated CP from CR3, consistent with their comparable initial resin coverage prior to any environmental exposure. However, by 72 h, the two panels had begun to diverge in a manner that directly parallels their quantitative water absorption trajectories: CP, which recorded 0.69 ± 0.0345% absorption at 72 h against CR3's 0.54 ± 0.027%, correspondingly displayed more extensive surface roughening, void formation, and partial fiber exposure in Figure 25 than CR3, whose surface retained a greater proportion of smoother matrix regions. This correlation between higher gravimetric water uptake and more advanced surface disruption is consistent with reports that moisture ingress into fiber-reinforced polymers manifests morphologically as progressive interfacial degradation and fiber exposure once sufficient water has permeated the near-surface region [16,22,23,24]. By 10 days, this divergence became most pronounced: CP exhibited harsh surface roughening, severe fiber exposure, interfacial bonding features, and voids, while CR3 showed comparatively less severe roughening alongside partial fiber exposure and the continued presence of smoother matrix regions, a morphological contrast that mirrors the absorption values recorded at this interval, where CR3 (0.954 ± 0.048%) remained below CP (1.010 ± 0.051%), and both remained substantially below CR1 (2.986 ± 0.149%). The non-monotonic absorption trajectory shared by all panels, characterized by an increase at 24 h, a decrease at 48 h, a subsequent increase at 72 h, and a substantial increase by 10 days, indicates that moisture uptake did not follow a simple monotonic trend. This behavior may reflect multiple moisture-transport and redistribution processes within the heterogeneous fiber–matrix structure [23,24]. Read together with Figure **24**, these observations suggest that the intermediate-interval fluctuations in bulk absorption may correspond to internal moisture redistribution before the visible onset of more severe surface roughening and fiber exposure, which becomes morphologically evident at later exposure times. The attenuated absorption, thickness-swelling reversal, and surface degradation observed for CR3 relative to CP and CR1 therefore converge on the same structural determinant identified in the tensile and tribological analyses: a more effectively bonded,

PET-bottle-derived fiber network restricts both moisture ingress pathways and the associated long-term surface and dimensional instability, extending a single fiber–matrix interfacial-integrity narrative across the mechanical, tribological, and hygroscopic domains examined in this study.

5. Conclusion

This study examined how the fiber source (virgin polyester, recycled textile waste, and recycled PET-bottle fiber) and non-woven bonding structure (needle punching alone vs. combined needle punching and thermal bonding) govern the tensile, tribological, and hygroscopic performance of compression-molded polyester composites and whether resin consolidation transmits or overrides the mechanical hierarchy set at the fabric stage. Key findings:

1. The relatively narrow range of reinforcement loading (29.7–33.9 wt%) indicates that the observed differences in composite performance were strongly associated with differences in fiber source, bonding structure, and reinforcement architecture under the investigated conditions.
2. The fabric-level tensile ranking (R3 > P > R2 > R1; e.g., 1701.93 N vs. 9.8–12.2 N in the Y-direction strip strength) was reproduced exactly at the composite level (CR3 > CP > CR2 > CR1), with CR3 reached the highest maximum tensile load of 2488 N and tensile toughness of 22,395 N in the Y-direction, while its maximum elongation reached 11.26% in the X-direction.
3. FE-SEM fractography confirmed this inheritance mechanism: the R3-derived CR3 panel, whose fabric achieved the highest bursting strength (2613.33 N) and puncture resistance (944.07 N), showed markedly less fiber/matrix debonding and matrix separation than the virgin-fiber CP panel, with failure shifting from debonding in the weaker cross-direction to fiber breakage with elongation in the stronger machine and diagonal directions.
4. All reinforced composites reduced wear relative to the unreinforced resin (1.85×10^{-3} cm^3 loss and 1.938 mm track width at 35 N), with CR2 being the most wear-resistant (0.665×10^{-3} cm^3); only 5.35% track

widening from 15to 35 N despite not being the strongest in tension, indicating sliding-wear resistance and bulk tensile capacity are partially independent properties.

5. FE-SEM analysis of the worn surfaces reinforced this interfacial-quality distinction: CP exhibited interfacial bonding cracks at both 15 and 35 N, increasing in extent with load, whereas CR3 showed no interfacial bonding cracks at either load level, indicating that the same fiber–matrix coupling limiting debonding under tensile loading also restrained crack initiation at the sliding contact interface.
6. CR1 (no thermal binder fiber) absorbed the most water at every interval (2.986% at 10 days) and showed the most severe short-term thickness contraction (−7.92% at 2 h) before reversing to the highest long-term swelling (2.28% at 10 days). CR3 consistently exhibited the most restrained absorption and dimensional response among the reinforced panels.
7. The FE-SEM images of the immersed surfaces tracked this divergence morphologically: CP and CR3 were indistinguishable at 0 h, but by 10 days, CP displayed harsh surface roughening, severe fiber exposure, and interfacial bonding degradation, whereas CR3 retained comparatively smoother matrix regions with less severe roughening and fiber exposure, directly mirroring their respective 10-day water absorption values (1.010% for CP vs. 0.954% for CR3).

Implications:

1. Thermally bonded PET-bottle-derived non-woven reinforcement can match or exceed virgin-fiber composite performance without requiring higher fiber loading.
2. Recycled PET non-wovens demonstrated potential as technically viable waste-derived reinforcements for polyester composites under the investigated conditions.
3. For circular economy composite manufacturing, prioritizing binder-fiber content and thermal-bonding quality during non-woven perform selection, rather than fiber source alone, offers a practical and scalable pathway for substituting recycled feedstocks into load-bearing, wear-resistant, and moisture-exposed applications while retaining competitive mechanical performance under the investigated conditions.

Data Availability

The authors declare that the data supporting the results of this study are available on paper.

Disclosure statement

The authors reported no potential conflicts of interest.

Funding

Open access funding provided by The Science, Technology & Innovation Funding Authority (STDF) in cooperation with The Egyptian Knowledge Bank (EKB).

Author contributions

E.M., D.H.E, W.A.H., and M.I.A.H. designed the study and conducted the experiments, E.M., D.H.E, W.A.H., and M.I.A.H. provided materials, E.M., D.H.E, W.A.H., and M.I.A.H. were involved in writing-original drat preparation, E.M., D.H.E, W.A.H., and M.I.A.H. was involved in writing-review and editing, E.M., D.H.E, W.A.H., and M.I.A.H. provided resources, supervision, and editing. All authors reviewed the manuscript.

References

[1] Das, T. K., Jesionek, M., Ali, M. D., Ganguly, S. & Poater, A. Advancing sustainability: circular economy strategies for fibrous polymer composites. Clean. Mater. 19, 100381 (2026). https://doi.org/10.1016/j.clema.2026.100381.

[2] Colledani, M., Turri, S., Diani, M. & Mathes, V. Introduction, context, and motivations of a circular economy for composite materials. In Systemic Circular Economy Solutions for Fiber Reinforced

Composites (eds Colledani, M. & Turri, S.) 1–15 (Springer, 2022). https://doi.org/10.1007/978-3-031-22352-5_1.

[3] Krauklis, A. E., Das, S. C., Agostino, P. & Grammatikos, S. Policies and guidelines for recycling of fiber-reinforced polymer (FRP) composites: current state, industrial practices and future perspectives. Macromol. Symp. 415, e70400 (2026). https://doi.org/10.1002/masy.70400.

[4] Mustafa, E. M. et al. Acoustical and mechanical properties of sisal and kenaf fibers reinforced composites. Industrial Technology Journal (2025). https://doi.org/10.21608/itj.2025.311635.1018.

[5] Enking, J. et al. Recycling processes of polyester-containing textile waste—a review. Resour. Conserv. Recycl. 219, 108256 (2025). https://doi.org/10.1016/j.resconrec.2025.108256.

[6] Park, S. H. & Kim, S. H. Poly (ethylene terephthalate) recycling for high value added textiles. Fashion Text. 1, 1 (2014). https://doi.org/10.1186/s40691-014-0001-x.

[7] Luedemann, L., Felber, A. & Golder, M. Development of a recycling process for textiles made from PET, and proof of its environmental preference with life cycle assessment. Int. J. Technol. Manag. 88, 134–154 (2022). https://doi.org/10.1504/IJTM.2022.121501.

[8] Todor, M. P., Bulei, C., Kiss, I. & Cioată, V. G. Recycling of textile wastes into textile composites based on natural fibres: the reinforcement type and the architecture. IOP Conf. Ser.: Mater. Sci. Eng. 477, 012055 (2019). https://doi.org/10.1088/1757-899X/477/1/012055.

[9] Badara, O., Rämö, V., Rissanen, M. & Tehrani-Bagha, A. Mechanically recycled textile fibers in carded and needle-punched non-wovens: implications on processability, structure, and performance. Text. Res. J. 95, 1617–1636 (2025). https://doi.org/10.1177/00405175241302482.

[10] Karmakar, S., Majumdar, A. & Butola, B. S. A sustainable recycling process and its life cycle assessment for valorising post-consumer textile materials for thermal insulation applications. Waste Manag. Res. 43, 749–761 (2025). https://doi.org/10.1177/0734242X241270933.

[11] Mustafa, E., Malek, A. S., Mohamed, H. K., Abd El-Aziz, M. Y. & Hashima, W. A. Effect of sustainable fibers' length on mechanical, acoustic, and physical properties of composite materials. J. Compos. Mater. 60, 1575–1586 (2026). https://doi.org/10.1177/00219983251389653.

[12] Hashima, W. A., Abd El-Aziz, M. Y., Mohamed, H. K. & Mustafa, E. Modifying 3D composite textiles as functional panels. J. Compos. Mater. 59, 511–524 (2025). https://doi.org/10.1177/00219983241295290.

[13] Gnaba, I. et al. Investigation about the effect of manufacturing parameters on the mechanical behaviour of natural fibre nonwovens reinforced thermoplastic composites. Materials 12, 2560 (2019). https://doi.org/10.3390/ma12162560.

[14] Arumugam, S. et al. A review on the effect of fabric reinforcement on strength enhancement of natural fiber composites. Materials 15, 3025 (2022). https://doi.org/10.3390/ma15093025.

[15] Monti, M. et al. Enhanced impact strength of recycled PET/glass fiber composites. Polymers 13, 1471 (2021). https://doi.org/10.3390/polym13091471.

[16] Hassanpour, B. & Karbhari, V. M. Characteristics and models of moisture uptake in fiber-reinforced composites: a topical review. Polymers 16, 2265 (2024). https://doi.org/10.3390/polym16162265.

[17] Papán, D., Lapašová, L. & Papánová, Z. Hybrid composite materials made of recycled PET and standard polymer blends used in civil engineering. Polymers 15, 3407 (2023). https://doi.org/10.3390/polym15163407.

[18] Singh, D. K. et al. Finite element modeling of the fiber-matrix interface in polymer composites. J. Compos. Sci. 4, 58 (2020). https://doi.org/10.3390/jcs4020058.

[19] Venkatesh, R. et al. Effect of fiber layer formation on mechanical and wear properties of natural fiber filled epoxy hybrid composites. Heliyon 9, e15934 (2023). https://doi.org/10.1016/j.heliyon.2023.e15934.

[20] Milosevic, M., Valášek, P. & Ruggiero, A. Tribology of natural fibers composite materials: an overview. Lubricants 8, 42 (2020). https://doi.org/10.3390/lubricants8040042.

[21] Parikh, H. H. Tribology of plant-based natural fiber reinforced polymer matrix composites—a short review. J. Nat. Fibers 20, 2172639 (2023). https://doi.org/10.1080/15440478.2023.2172639.

[22] Melo, R. Q. C., Lia Fook, M. V. & Lima, A. G. B. Non-Fickian moisture absorption in vegetable fiber reinforced polymer composites: the effect of the mass diffusivity. Polymers 13, 761 (2021). https://doi.org/10.3390/polym13050761.

[23] Melo, R. Q. C., Lia Fook, M. V. & de Lima, A. G. B. Non-Fickian moisture transport in vegetable-fiber-reinforced polymer composites using a Langmuir-type model. Polymers 12, 2503 (2020). https://doi.org/10.3390/polym12112503.

[24] Tezara, C. et al. The effect of hybridisation on mechanical properties and water absorption behaviour of woven jute/ramie reinforced epoxy composites. Polymers 13, 2964 (2021). https://doi.org/10.3390/polym13172964.